Project Title: **3D Printed, Low Tortuosity Garnet Framework For Beyond 500 Wh/kg Batteries**

Award number: **DE-EE0008201**

Sponsoring program office: **Office of Energy Efficiency & Renewable Energy**

Technical Contact:
Eric Wachsman
1206 Engineering Laboratory Building
University of Maryland
College Park, MD 20742
Phone: 301-405-8193
Email: ewach@umd.edu

Business Contact:
Stephanie Swann
Contract Manager
University of Maryland
Office of Research Administration | Room 3112 Lee Building
7809 Regents Drive| College Park, MD 20742
Phone: 301-405-6269 | Fax: 301-314-9569
Email: oraa@umd.edu

Organizations

University of Maryland, College Park, MD 20742

Team members

Principle Investigator:	Eric Wachsman
Co-Principle Investigator:	Liangbing Hu

Table of Content

Abstract

In this project, we developed LLZO garnet ink recipes and processes for 3D-printing highly ordered ionically conductive garnet porous structures on dense garnet separators. Using this technique, we are able to fabricate controlled architecture LLZO garnet solid-state electrolyte (SSE) trilayers for application in solid-state lithium batteries. The trilayer comprises a thin dense center layer sandwiched between a 3D-printed patterned porous layer and a random porous layer. The dense layer functions as the ionic separator between the anode and cathode. The random porous layer hosts the lithium-metal anode and provides the structural support. The 3D-printed SSE patterned porous layer hosts the cathode, providing continuous, low tortuosity pathways for fast 3D Li^+ transport through the cell while increasing the electrode/electrolyte interface area to decrease the interfacial resistance. Compared to the random porous structure, this ordered patterned structure possesses more vacant space for higher cathode loading without sacrificing ionically conducting capability, thus potentially greatly increasing the cell energy density. For demonstration purposes, we developed two patterns for the 3D-printed porous layer: grids and columns, for hosting sulfur and NMC cathode, respectively. The corresponding two types of cells were fabricated and tested, and have demonstrated achievement of theoretical discharge capacity without cathode calendaring. In addition, we developed a fundamental solid-state ionic and electronic transport model to optimize the 3D-printed structures for maximum energy and power density. The model was validated by experiment and provides the critical design criteria for achieving the >500 Wh/kg energy goal as function of C-rate.

Introduction

Lithium metal anodes are considered the Holy Grail for high-energy density batteries because lithium has the most negative electrical potential (-3.04V vs. SHE) and highest theoretical capacity (3860 mAh/g). Similarly, sulfur cathodes have an exceptionally high capacity at 1675 mAh/g. When a sulfur cathode is used with lithium metal, a high energy density lithium-sulfur battery is possible, with a theoretical energy density up to 2200 Wh/kg.[1] However, using lithium metal in organic liquid electrolyte systems face extensive challenges in terms of both battery performance and safety.[2]

Chemical and physical short circuits are two primary challenges in current lithium-sulfur batteries.[1] Polymer separators cannot effectively prevent chemical or physical short circuits. The dissolved active materials will inevitably travel though the polymer membrane micropores, and high modulus Li dendrites will easily penetrate the membrane. These short circuits compromise battery performance and safety. Solvation of active cathode materials and shuttling of unwanted chemical species in the liquid electrolyte result in "chemical short circuits", which deteriorate the electrodes and limit the deployment of new cathode materials, such as high voltage oxides and high capacity sulfur. To prevent chemical short circuits, extensive studies have focused on cathode nanostructure design, separator modification, and electrolyte additives, to alleviate active materials diffusion and shuttling. At the anode, Li dendrite penetration through the separator causes internal electronic, or "physical", short circuits. Several attempts to detect, delay, confine, or block Li dendrite penetration have been reported to extend cycle life and avoid thermal runaway in lithium-metal batteries, but are these permanent solutions?

A fundamental strategy to mechanically suppress lithium dendrites and intrinsically eliminate solid electrolyte interphase (SEI) formation is to deploy solid-state electrolytes (SSEs).[3-7] Among the different types of SSEs, solid-polymer electrolytes have been the most extensively studied.[8-13] In polymer-based composite SSEs, nanoparticles are incorporated to influence the recrystallization kinetics of the PEO polymer chains to promote local amorphous regions, thereby increasing the Li salt/polymer system's ionic conductivity. The fillers can be either non- Li^+ conductive nanoparticles, such as Al_2O_3, SiO_2, TiO_2, ZrO_2, and organic polymer spheres, or Li^+ conductive nanoparticles, such as $Li_{0.33}La_{0.557}TiO_3$, and $Li_{1.3}Al_{0.3}Ti_{1.7}(PO_4)_3$. Developing nanostructured fillers is an essential approach to increase the ionic conductivity of composite electrolytes due to the increased surface area of the amorphous region and improved interface between fillers and polymers.

In addition, numerous solid-state inorganic Li^+ electrolytes are being investigated due to their high ionic conductivity and excellent stability, Li-stuffed garnets exhibit the most promising physical and chemical properties for SSEs. However, major challenges still exist in garnet based electrolytes, particularly high interfacial impedance between electrodes and garnet electrolyte. Until our recent work, major challenges limited garnet SSE performance, namely the inability to reduce electrolyte thickness to practical levels (<50 μm), and high Li-garnet interfacial impedance, both of which severely limited achievable current density. Before starting the current EERE project, we had already overcome the solid-electrolyte/solid-electrode interfacial impedance using various interface materials with garnet (e.g. $Li_7La_3Zr_2O_{12}$, LLZ) solid-state electrolytes (SSEs) under BMR contract DEEE0006860, and we had developed thin (~10 μm) LLZ SSEs on high surface area random porous LLZ support structures under ARPA-E contract DE-AR0000384 achieving an areas specific resistance (ASR) of only 2 Ω-cm^2 at a record high current density of 10 mA/cm^2.[14] We had also successfully demonstrated full batteries with Li-metal anodes and $LiCoO_2$, $LiMn_2O_4$, and S cathodes. The Li-S batteries using the random porous garnet architecture, with 100 μm thick S-cathodes and capacity matched Li-anodes, reached ~300Wh/kg (full cell mass) under NASA support. We were on a clear path to achieve 500 Wh/kg (full cell mass) through improved S utilization with the ~100 μm thick electrodes.

Based on our achievements mentioned above, for the current project, we proposed to extend our success to 3D printed low-tortuosity garnet frameworks to achieve far beyond 500 Wh/kg batteries by optimizing the

electrode microstructure, enabling higher C-rates and thicker electrodes (~200 μm). The difference between the proposed garnet framework with that used in our previous projects lies in the porous layer. The 3D printing method produces ordered low tortuosity and higher porosity (~85%) garnet structures, thus enabling higher Li^+ and electron charge transport for higher rate performance, ease of battery fabrication (Li and S/C infiltration), and dramatically higher areal electrode capacity. The resulting enhanced charge transport and ease of electrode infiltration will allow us to dramatically increase electrode thickness and thus obtain even higher energy density. Moreover, with controlled 3D framework structures we can optimize not only C-rate and energy density, but also mechanical strength (e.g., pillar vs. grid structures). The corresponding electrochemically and mechanically optimized garnet framework by 3D printing will revolutionize solid-state metal-anode battery technology.

Project objectives: This project aims to fabricate controlled 3D porous solid state electrolyte structures that are ordered and act as electrode supports, facilitating fast ion transport within the electrodes. This will enable higher battery C-rates and thicker electrodes for higher loading. The 3D structures can also increase the mechanical strength of the solid-state battery. In parallel, 3D solid-state ionic and electronic transport models will be developed to determine achievable C-rates as a function of structure. With this information, high performance Li-S and Li-NMC batteries will be fabricated using the 3D solid state electrolyte structures (Figure 1).

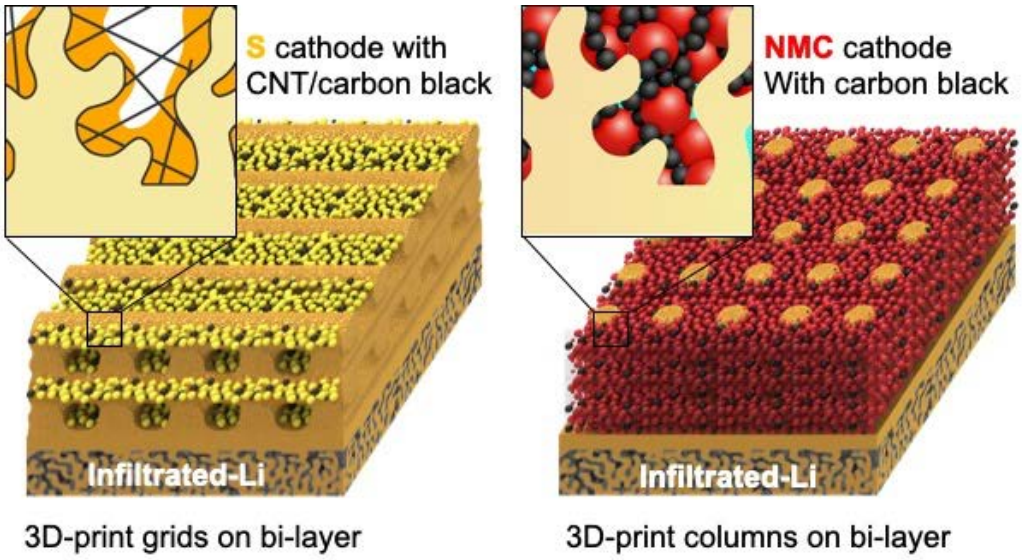

Figure 1. Schematic of sulfur (S) and NMC cathode chemistries in 3D printed grid and column structures, respectively, on dense-porous bilayer garnet with capacity matching Li metal filled in the random porous bottom layer.

Approaches: LLZ garnet inks were developed to 3D-print solid electrolyte high porosity, low tortuosity patterns, including lines, grids, and columns. Using 3D-printing enables the rapid comparison of different electrolyte structure types as well as variations in structure characteristics (column height, width, etc.). These structures were used in porous-dense-porous trilayer structures and assembled into batteries for testing. In addition, 3D solid-state ionic and electronic transport models were developed to understand how the 3D structure effects the ionic and electronic transport rates and how we can increase electrode loading while maintaining high C-rates. The models were validated by experiment and used to optimize the 3D electrolyte structure.

The specific tasks and milestones and the corresponding achievements are summarized below for Phase I and Phase II, respectively.

Achievements in Phase I

Task 1: Design and fabricate low-tortuosity porous-dense-porous garnet frameworks

Milestone 1.1: Develop stable garnet ink with well dispersed garnet particles

Lithium garnet powder with the composition $Li_{6.75}La_{2.75}Ca_{0.25}Zr_{1.5}Nb_{0.5}O_{12}$ (LLZ) was synthesized by solid state reaction. XRD results show pure cubic phase garnet in Figure 2a. The powder was then ball-milled in multiples steps with decreasing sizes of media to reduce the particle size. The d_{90} of the powder was 255 nm which is suitable for 3D-printing (Figure 2b). The ink was then mixed with an ESL binder and 200 proof ethanol to create 3D-printing inks. Several series of inks were made to test effect of the ratio of binder, garnet, and solvent concentration on viscosity. Two garnet:binder ratios were chosen (2.08:1 and 1.85:1). To these mixtures 15-50 wt% solvent was added. Figure 3 shows the rheological properties of the different inks. Figure 3a and b show the inks with garnet:binder ratios of 2.08:1 and 1.85:1, respectively. The different solvent fractions are indicated by percent in the plots. The ink with the least amount of binder (2.08:1 garnet:binder) and solvent (18% ethanol) and therefore the highest solids loading was unstable (Figure 3a, orange line). All other inks were stable and had viscosity values from 345 cP to 52,000 cP. The most viscous ink (Figure 3b, purple line) displayed some shear-thinning behavior as well due to the higher amount of binder and limited amount of solvent used. The inset photo in Figure 3b shows how the high viscosity ink retains its shape after exiting the nozzle of the syringe.

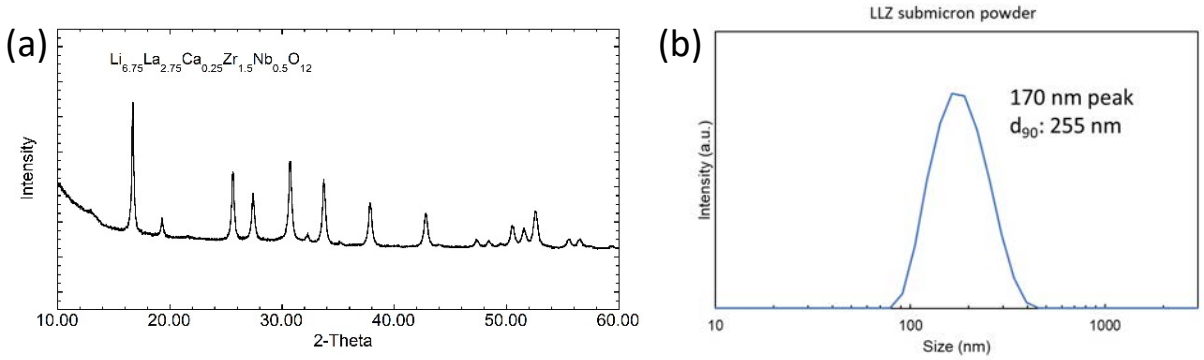

Figure 2. Particle size distribution of LLZ powder used for printing.

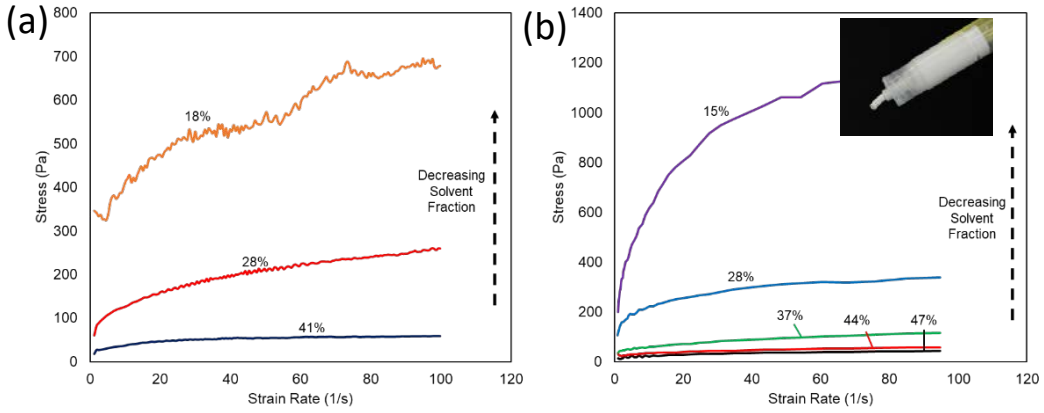

Figure 3. Rheological data for 3D-printing LLCZN garnet inks with a garnet:binder ratio of (a) 2.08:1 and (b) 1.85:1. The solvent wt% is indicated on each line.

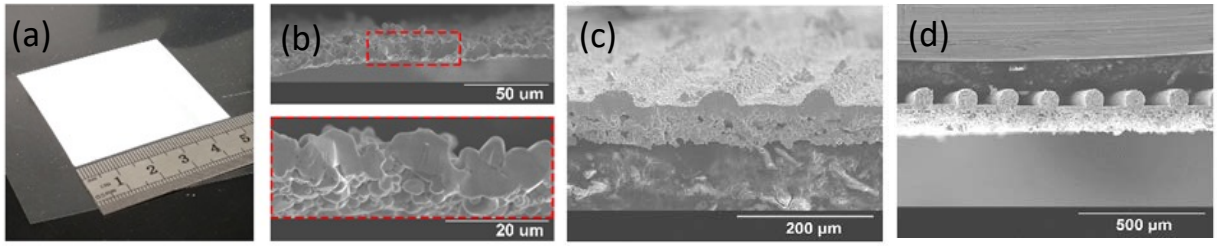

Figure 4. (a) Photograph of 5x5 cm single layer thin film of 3D-printed low viscosity LLCZN ink. (b) SEM cross-sectional image of sintered film. SEM cross-sectional images of sintered LLCZN line patterns printed with (c) low viscosity conformal ink and (d) high-viscosity self-supporting ink.

Milestone 1.2: Print line array structure and column structure

The stable inks were used for the 3D-printing of LLCZN. Low viscosity inks were used to print a single layer of a large-area uniform film. An example single layer film is shown in Figure 4a. The film was then sintered to yield a film of pure LLCZN garnet with a thickness of only 5-10 µm (Figure 4b). Varying line patterns were also printed to produce high surface area, open porosity structures. The patterns were printed onto a LLCZN tape substrate, which after sintering would serve as the electrode-separating dense layer of the cell. Low viscosity inks were first compared to high-viscosity inks. Figure 4c and d show cross-sectional SEM images of line patterns printed on LLCZN substrates using a low viscosity, more conformal ink (Figure 4c) and a higher viscosity self-supporting ink (Figure 4d). The lower viscosity ink results in a line which partially conforms to the surface, observed by the low contact angle. In contrast, the higher viscosity ink wets the substrate much less, and the lines maintain a round shape. Additional variations in the line pattern dimensions are shown in Figure 5. Line widths of 200, 220, and 285 µm and line separations of 110, 200, 260 µm were achieved, demonstrating control over the 3D-printing process.

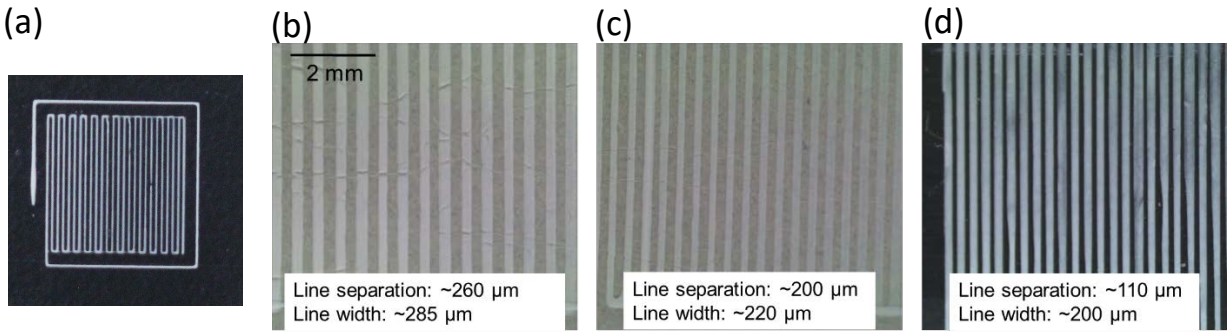

Figure 5. Images of 3D-printed LLCZN garnet inks. (a) Photograph of a typical print area. (b-d) Microscope images of line patterns with varying line thickness and separation by tuning the raster pattern and other printing variables.

Garnet columns of varying diameter and height were 3D-printed onto a garnet tape substrate. The print areas were 1 x 1 cm or greater with 0.5-1 mm center to center column spacing. Photographs of the prints are shown in Figure 6. Columns were printed with diameters from 300 µm to ~75 µm and heights ranging from 50-200 µm. The largest aspect ratio achieved was ~2.0. These values were measured before sintering, where significant shrinkage occurs due to binder burnout and densification of the garnet. Figure 6 shows SEM images of the sintered 3D-printed columns. The maximum height of a sintered column was measured to ~180 µm with a diameter of ~100 µm, representing an aspect ratio of 1.8.

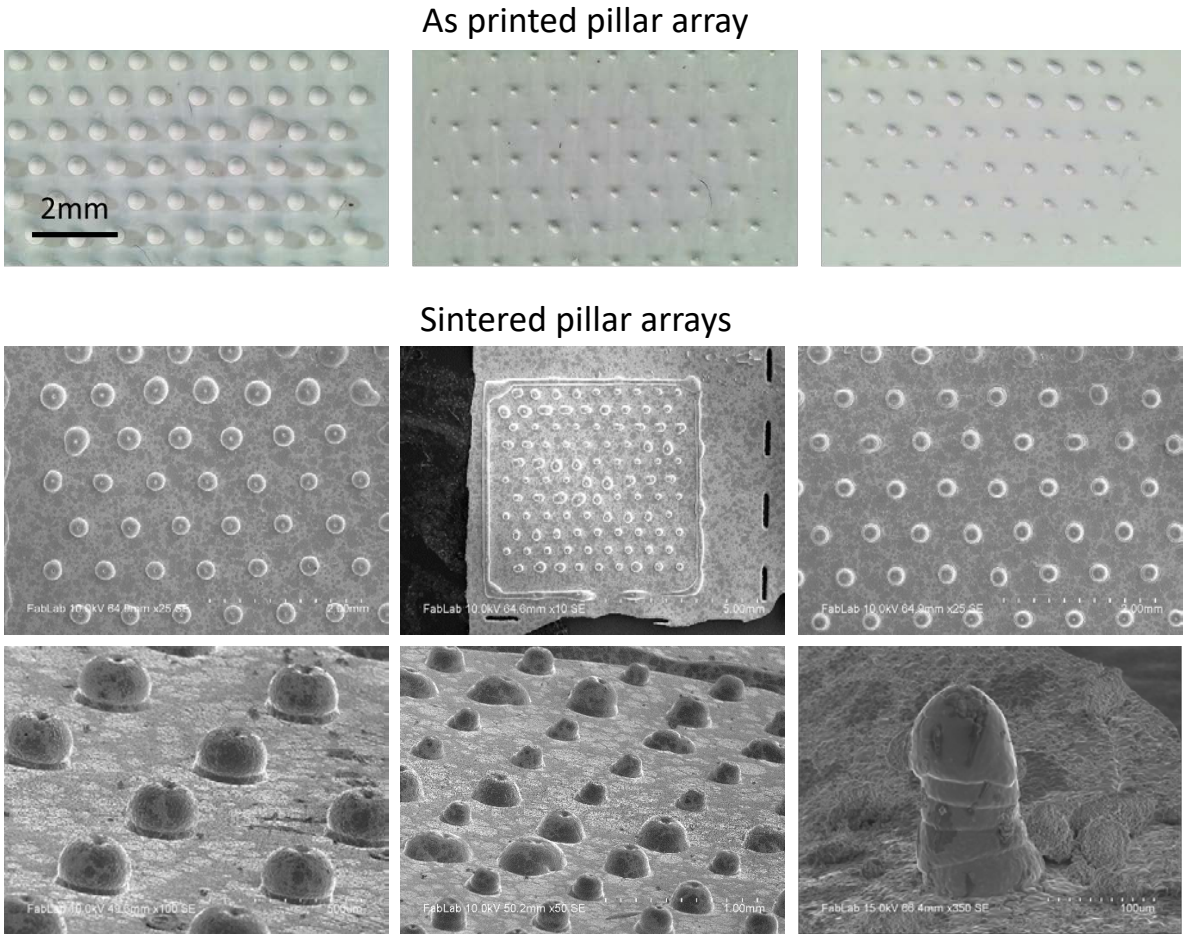

Figure 6. Photographs of as-printed (top) and SEM images of sintered (bottom) 3D-printed multilayer pillar structures on garnet substrate with aspect ratio 0.65-1.8

Milestone 1.3 Print multilayer grid structure

The ink formulations were able to be tailored to optimize rheological properties for self-supporting structures such as the multilayer grid structures. Additionally, carefully controlling the drying rate has been a very important consideration to prevent structure degradation between printing and sintering. Control over the 3D printing process has shown improvement through the successful prints of the 3D multilayer grid structures. Using these inks, overlaid orthogonal raster patterns were printed in 1 x 1 cm areas on garnet substrates as seen in Figure 7 to create multilayer grid structures. Post sintered structures had line-to-line distances varying from 275 µm to ~315 µm with line thicknesses ranging from 90-200 µm.

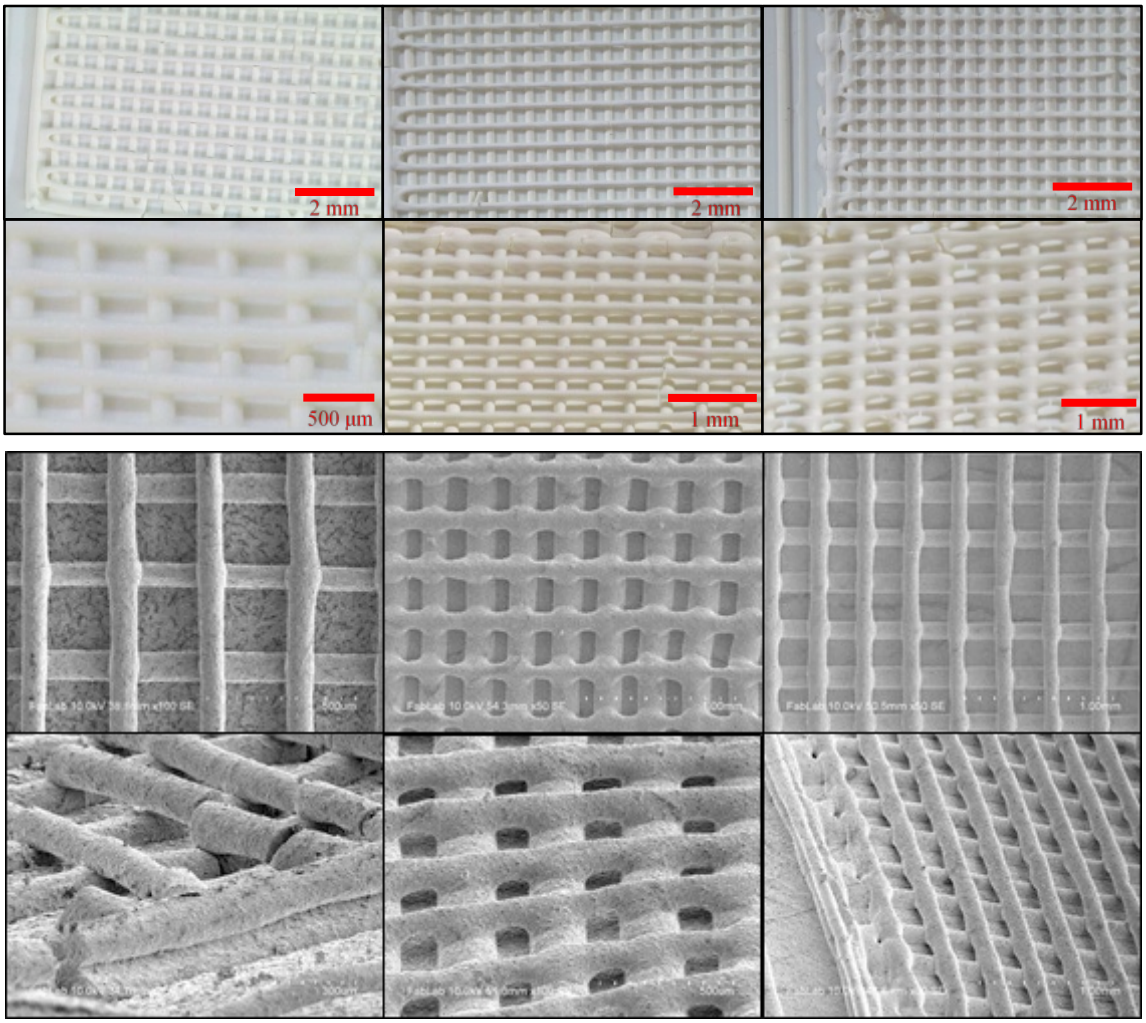

Figure 7. Photographs of as-printed (top) and SEM images of sintered (bottom) 3D-printed multilayer grid structures on garnet substrate.

Task 2: Develop transport and capacity models

Milestone 2.1 Develop theoretical models to predict the performance of the Li-S full cell

Construction of a theoretical model to predict the performance of the 3D-printed structures and the transport properties began with a two-dimensional approach. Figure 8 below shows the basic concepts used in the modelling of the column structures. The first component demonstrates the driving forces due to chemical concentration gradients and resulting diffusion. The second component is the electrical migration of ions caused by the electric field. These two components have somewhat different profiles which overlap to create the overall lithium concentration profile as a function of charge state.

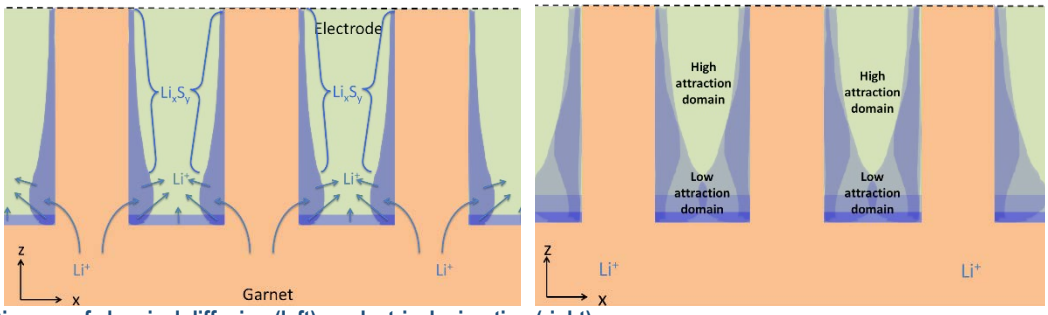

Figure 8. Diagram of chemical diffusion (left) vs electrical migration (right).

Figure 9 shows the concentration profile within the electrode between the garnet pillars as function of charge state. There is clearly a dependence on the height of the column as well as the column separation. **Figure 10** shows the lithium transport within the garnet pillars with varying pillar diameter, which also has an effect on the rate at which lithium can access the electrode.

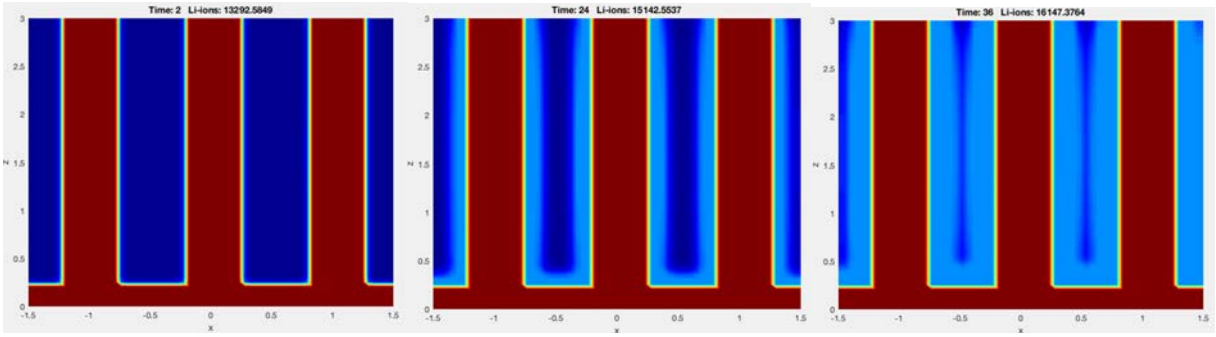

Figure 9. Visualization of the Li concentration within the electrode (initially dark blue) as the cell is discharged. The initial state (charged) is shown on the left and discharged towards the right.

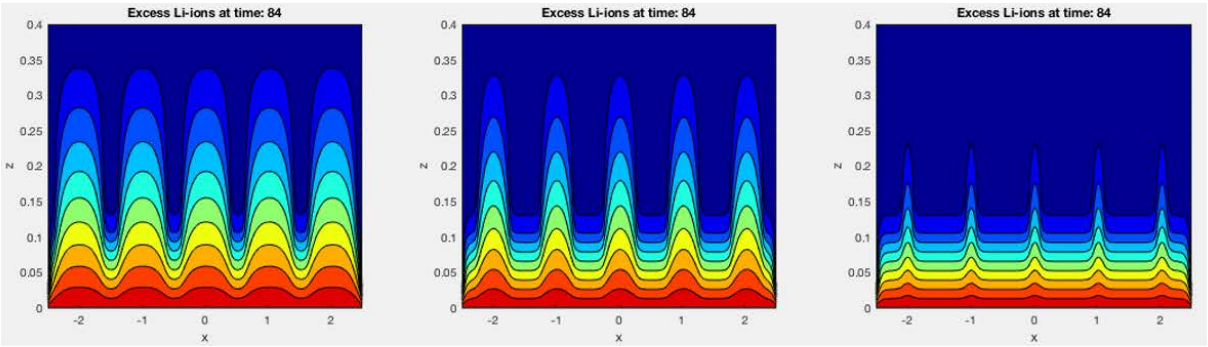

Figure 10. Diagram of lithium transport within the garnet pillars during discharge.

This model tracks the movement of lithium ions through the electrolyte and sulfur electrode by considering the physical forces that affect each lithium ion – chemical diffusion and electromagnetic forces.

Chemical Diffusion

In thermodynamics, concentration-related diffusion is described with a probabilistic model of fluxes.

$$J = -D\nabla c$$

Where flux, J, is related to the first spatial derivative of concentration, c, by a diffusion coefficient D. When combined with an equation maintaining that mass is conserved in the system:

$$0 = \frac{\partial c}{\partial t} + \frac{\partial J}{\partial x}$$

The equation can be rewritten in the more recognizable heat-wave equation (Fick's second law).

$$\frac{\partial c}{\partial t} = D_c \nabla^2 c$$

Electrical Diffusion

In addition to the random walks of particles in a concentration gradient, the lithium ions in our system also experience the pull of electric potentials. The potential at a specific point is determined by the stoichiometry of the electrode at that point, or the amount of lithium in the Lithium polysulfide. The potential of each polysulfide is determined experimentally and is shown in Figure 11.

$$J_{electrical} = -\frac{DzF}{RT} c(\nabla \phi)$$

Where z is the number of charges associated with the moving ion (z=1 for Li-ions), F is the Faraday constant, R is the ideal gas constant and ϕ is the electrochemical potential at a voxel. This potential of an entire voxel is determined by taking the lithium concentration in the voxel as an average for that area and assigning that potential to the lithiation contour in Figure 11.

The total concentration change can be determined after combining all flux equations to a net flux term:

$$J_{net} = J_{chemical} + J_{electrical}$$

$$J_{net} = -\left[D\nabla c + \frac{DzF}{RT} c(\nabla \phi)\right]$$

$$\boldsymbol{\frac{\partial c}{\partial t} = D\left[\nabla^2 c + \frac{zF}{RT}\left(\nabla c \nabla \phi + c\nabla^2 \phi\right)\right]}$$

This model utilizes a discrete, iterative approach to calculating the concentration of lithium ions, and in turn lithium polysulfides over the entire 3D volume.

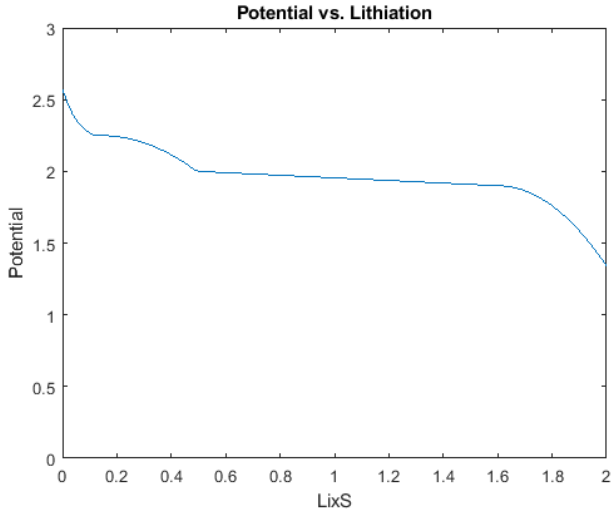

Figure 11. Lithiation curve used to determine the potential of a given voxel as determined by the average lithium.

First, a 3D array was created where each cell represents one of thousands of cubic voxels. Each cell is populated with an object that stores information that pertains to that position such as the material that is most prevalent (electrode or electrolyte), the amount of lithium, the charge associated with that lithiation, and the diffusion coefficient. This array is then evaluated cell-by-cell, considering the effect that nearest-neighbors sites have on ion motion into and out of the cell in question. These changes are then applied to

every cell in an iterative fashion. The evaluation and application are separated into two different processes to avoid any issues with delay of information propagation. This process is shown in Figure 12.

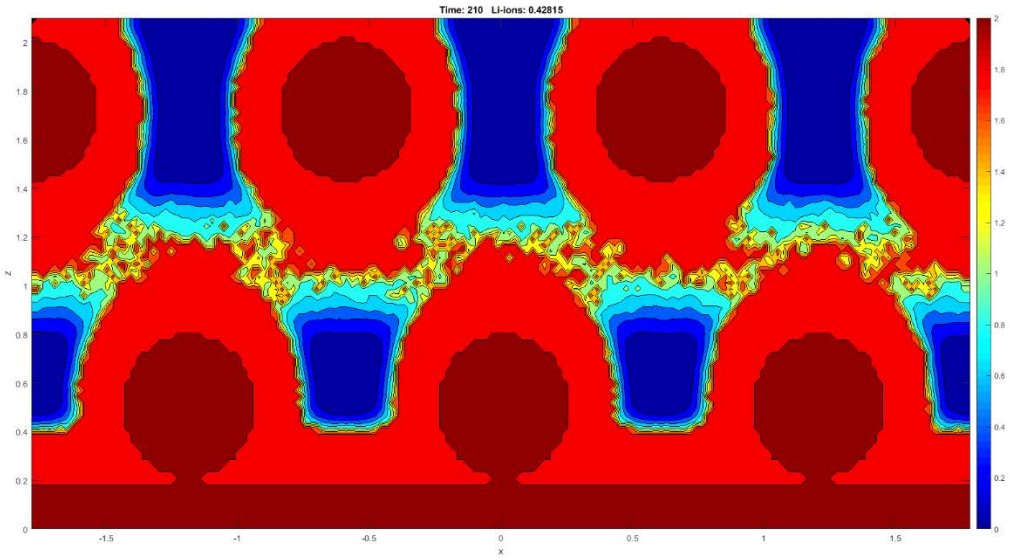

Figure 12. Effect of electrolyte features out of the of the cross section.

Initial lithium concentrations are 0 for electrode domains and 6.75 for electrolyte domains as dictated by stoichiometry. After considering the relative densities of Sulfur and garnet, the number maximum of lithium atoms contained in a given voxel are comparable.

Continuous to a discrete model

Any jump from a continuous model to a discrete one will come with a small amount of over/under estimation; however, the dynamics and core concepts behind the model will remain the same. In our equation for concentration there are five continuous components that need to be made discrete – the time step, dt, the first and second order spatial derivatives of concentration, ∇c and $\nabla^2 c$; and the first and second order spatial derivatives of potential, $\nabla\phi$ and $\nabla^2\phi$. Breaking up the calculations into an iterative algorithm automatically sets the time step. Because information about concentrations travels one block at a time, the rate-limiting step is dependent on the number and therefore size of the blocks. The higher spatial resolution the model is, the smaller each time step, dt. The process of transforming a continuous space to a discrete space is relatively straightforward. For any given characteristic, ν, in one dimension:

$$\nabla\nu \overset{1D}{=} \frac{d}{dx}\nu$$

$$\nabla^2\nu \overset{1D}{=} \frac{d}{dx}\left(\frac{d}{dx}\nu\right)$$

Where, if dx = 1 for a unit size:

$$\frac{d\nu(x)}{dx} = \frac{\nu(x+1) - \nu(x) + \nu(x) - \nu(x-1)}{2\,dx}$$

$$d\nu = \frac{1}{2}\big(\nu(x+1) - \nu(x-1)\big)$$

$$\frac{d}{dx}\left(\frac{d}{dx}v\right) = \frac{d}{dx}\left(\frac{v(x+1) - v(x) + v(x) - v(x-1)}{2\,dx}\right)$$
$$d^2v = v(x-1) + v(x+1) - 2v(x)$$

The same process can be used for any Cartesian coordinate and is scaled to higher dimensions by linearly combining the equations for each additional dimension. In 3D, these derivatives can be treated as arrays:

$$\nabla_{3D} = \begin{bmatrix} 0 & 0 & 0 \\ 0 & -0.5 & 0 \\ 0 & 0 & 0 \end{bmatrix}_{-1}, \begin{bmatrix} 0 & 0.5 & 0 \\ -0.5 & 0 & 0.5 \\ 0 & -0.5 & 0 \end{bmatrix}_{0}, \begin{bmatrix} 0 & 0 & 0 \\ 0 & 0.5 & 0 \\ 0 & 0 & 0 \end{bmatrix}_{1}$$

$$\nabla^2_{3D} = \begin{bmatrix} 0 & 0 & 0 \\ 0 & 1 & 0 \\ 0 & 0 & 0 \end{bmatrix}_{-1}, \begin{bmatrix} 0 & 1 & 0 \\ 1 & -6 & 1 \\ 0 & 1 & 0 \end{bmatrix}_{0}, \begin{bmatrix} 0 & 0 & 0 \\ 0 & 1 & 0 \\ 0 & 0 & 0 \end{bmatrix}_{1}$$

The relation between discharge rate and printed feature size was simulated, using a fixed porosity of 85% and cathode thickness of 200 µm. These values fix the cathode loading, and thus the energy density. Based on modeled cell design parameters this is projected to be 900 Wh/kg, significantly exceeding the Battery 500 goal. The model results, shown in Figure 13, are useful in this case to determine what structure and dimensions are needed to achieve sufficient power densities for this thickness of cathode. For comparison, a bilayer with no 3D-printed structure was also modeled and included in Figure 13. Overall, the models show that any printed structure utilizes the electrode at a much faster rate than a bilayer, and that as feature sizes decrease electrode utilization rate correspondingly increases. Further analysis of the relative power density is shown in Figure 13c, which plots the relative C-rate as a function of feature diameter using a bilayer (generally limited to C/10) as the baseline. The results suggest that in general the columns have somewhat higher power density than the grid structures, as they provide more direct ion pathways across the cell. Additionally, with feature diameters below ~30 µm C-rates >1 are attainable, and below 10 µm, rates over 3C is possible. Smaller features have clear advantages for cell performance.

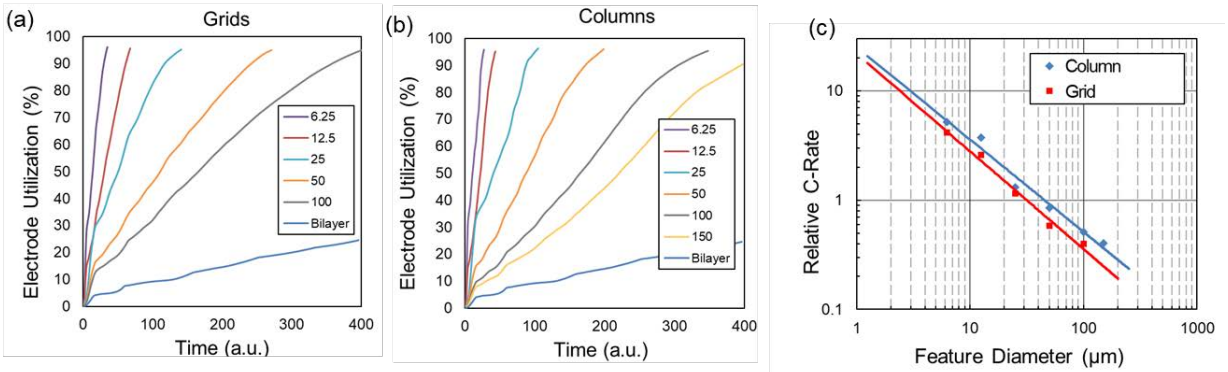

Figure 13. Modeling of electrode lithiation as a function of time using a fixed electrode loading (by fixing 85% electrolyte structure porosity and 200 µm height) and varying feature diameters for the (a) grid and (b) structures. (c) Relative power densities of these structures as function of feature diameter.

Figure 14 shows the modeling results for some of the 3D-printed structures that have been demonstrated thus far. Specifically, grid structures with 75 µm line diameters and 2-layer height (150 µm) with line-to-line spacing of 300 and 500 µm, resulting in layer porosity of 80% and 89%, respectively; a column structure with 150 µm diameter columns with 225 µm height, and column separation of 500 µm (93% porosity), along with a bilayer for comparison. While these results clearly demonstrate the benefit of the

3D-printed structures to power density, it is also worth noting that energy density in each of these cases is 700-1000 Wh/kg, significantly above the 500 Wh/kg goal of the project.

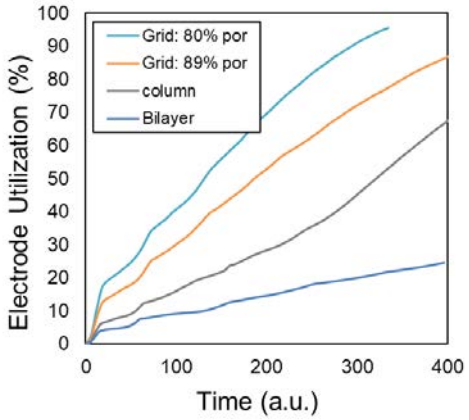

Figure 14. Modeling of select demonstrated 3D-garnet structures from Figure 6 and Figure 7: 2-layer grid structures with 75 µm feature diameter and 300 µm and 500 µm spacing (80 and 89% porosity, respectively), column structure with 150 µm diameter, 225 µm height, and 500 µm spacing (93% porosity), and a bilayer for comparison.

Task 3: Fabricate optimized full cells and demonstrate targeted performance

A full cell using NMC cathode was fabricated as follows: Using a non-Newtonian ink of garnet particles, a 2-layer garnet grid structure was 3D-printed on the dense layer of a porous-dense bilayer garnet electrolyte. The structure was then sintered, fusing the grid particles together and to the bilayer. The lines composing the grid structure have diameters of approximately 75 µm and a horizontal center-to-center spacing of 385 µm, equating to a layer porosity of 85%. Li metal was filled into the random porous layer on backside of the bilayer, while commercial 811 NMC powder, PVDF, and carbon black were filled into the grid structure with NMP as solvent. The total NMC loading was 14 mg/cm^2. The cell cycling results are shown in Figure 15. The impedance measurements in Figure 15a show a high resistance at room temperature, but it drops dramatically when heated to 60 °C, a temperature at which solid state batteries are quite stable. At a charge/discharge rate of C/20 (10 mA/g) a near theoretical discharge capacity (200 mAh/g) of 185 mAh/g is achieved. After five cycles, the rate was increased to C/7 (30 mA/g) and capacity decreased slightly to 170 mAh/g. The cell energy density of 120 Wh/kg is lower than desired, but due to several issues each of which we address in the Phase 2 proposal: (1) the grid structure is difficult for complete NMC particle infiltration and better suited for S electrodes (NMC is better suited for the column structure); (2) the 75 µm printed features are much larger than desired resulting in unecessary SSE cathode mass; (3) the electrode area is significantly smaller than the bilayer substrate, and thus only a fraction of the garnet material present is active in the cell; and (4) a thicker bilayer was used for mechanical support, contributing more garnet and lithium anode material than necessary. Thus there is signficant excess mass which will be removed in subsequent cells. On the other hand, the near theoretical capacity and high cycling efficiency demonstrate that the 3D-printed grid structure is of the correct garnet phase providing the desired 3-D ionic pathways through the electrode, and with the proposed Phase 2 improvements significantly higher energy density should be achieved.

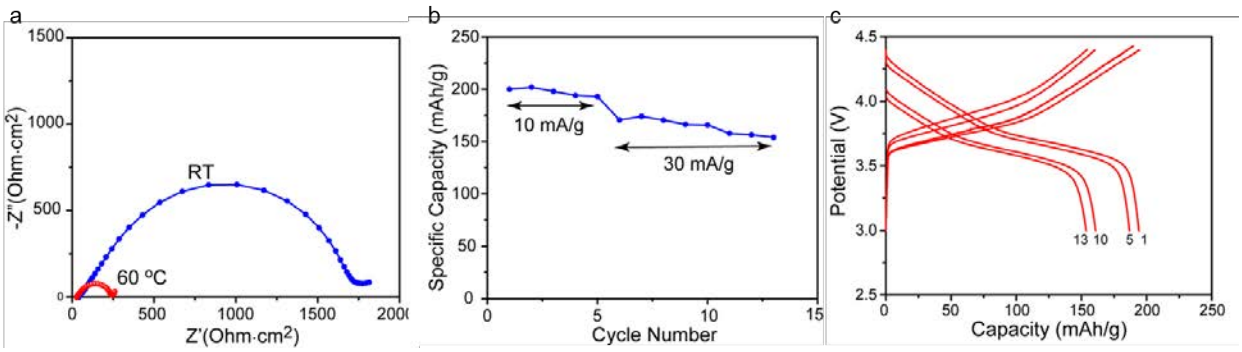

Figure 15. Electrochemical performance of Li-NMC battery at 60°C using a 2-layer grid structure on the cathode side with mass loading of about 14 mg/cm2 NMC and a current density of 10-30 mA/g. (a) EIS of the full cell at room temperature (blue) and at 60°C (red). (b) Discharge capacity vs cycle number. (c) Voltage profiles of select cycles 1 and 5 (10 mA/g), as well as 10 and 13 (30 mA/g).

Achievements in Phase II

Task 1: Optimize 3D Printed Low-Tortuosity Layer on Bilayer Garnet

Milestone 1.1 Increase SSE grid cathode structure height to achieve model design

We developed ethyl-cellulose dissolved in alpha-terpineol as a new binder system for the garnet inks to improve consistency and green strength. By keeping the Alpha-terpineol ratio to < 9 wt% and adding 3 wt% butanol in the ink to control rheological properties, we were able to reduce the inks' interaction with the green bilayer tapes as well as improving their self-supporting nature. We have successfully engineered a self-supporting ink capable of achieving smooth and dense 3D printed structures and enables reduced feature spacing by improving the printability with smaller printer nozzles. The consistency in the ink has greatly improved, and we have been able to print up to triple layered grid structures consistently, as displayed in Figure 16. The improved LLZ inks have also improved the sintered grid structures quite substantially allowing us to reduce the line width to 50 µm and the line separation to 139 µm in both the bottom layer and the suspended layer as seen in Figure 17.

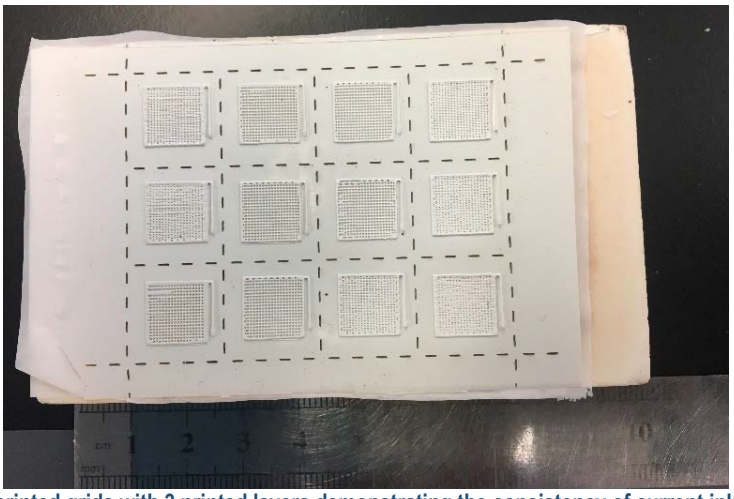

Figure 16. Showcase of 12 printed grids with 3 printed layers demonstrating the consistency of current ink composition.

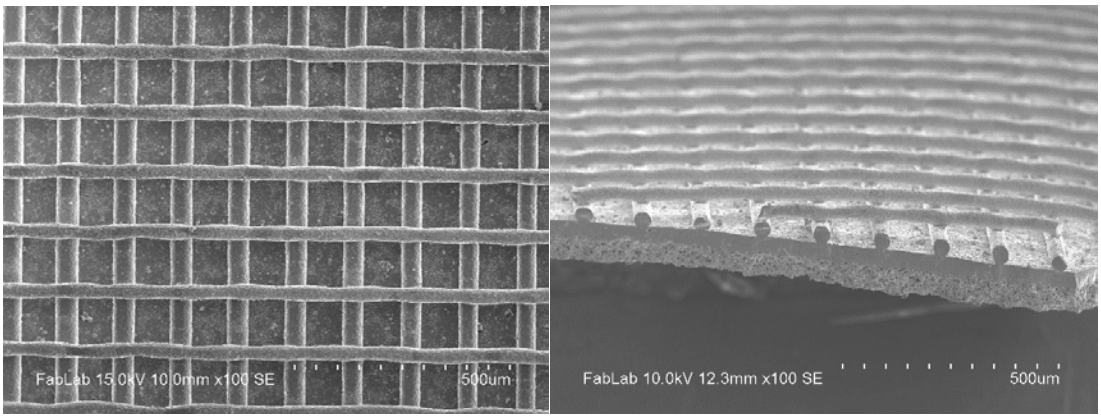

Figure 17. Left: Top-down image and Right: cross-section/side view of the 3D-printed grid structure using the optimized ink formulation. The grid structure has two layers with 139 µm line to line spacing and 50 µm diameter lines).

Milestone 1.2 Increase SSE column cathode structure height to achieve model design

With the improved ink, we were also able to print well-defined and clean column structures as shown in Figure 18a and b. The printing process is consistent over a print area of 8×8 mm for one print and scalable for multiple prints on multiple bilayer green tape pieces as seen in Figure 18c. The SEM of the sintered print in Figure 19 demonstrates that both the dense layer of substrate and the printed columns sinter very dense and flat, which indicates that reducing the contact surface area with the current ink and bilayer was effective at promoting sintering. Figure 19a and b indicate the sintered columns are 56-62 µm diameter and 207-215 µm in height (aspect ratio = 4.0) which meets the model design maximum column height, i.e., electrode thickness (200 µm). The spacing between columns is ~300 µm. Taking this one step further, we have been able to increase the column height without sacrificing the aspect ratio of the column. Figure 19c and d indicate the sintered columns are 110 µm diameter and 350 µm in height.

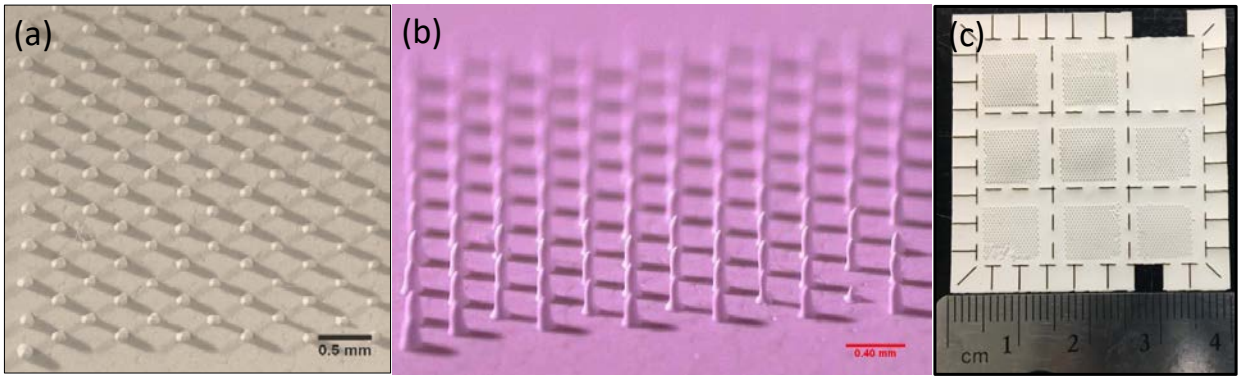

Figure 18. Optical microscope images of green print of 3D columns on top of bilayer green tapes. (a) directly overhead image; (b) angled overhead image; (c) multiple prints on multiple bilayer pieces. The printed dimensions of each individual print are 8x8 mm. Top right sample was left unprinted as a control.

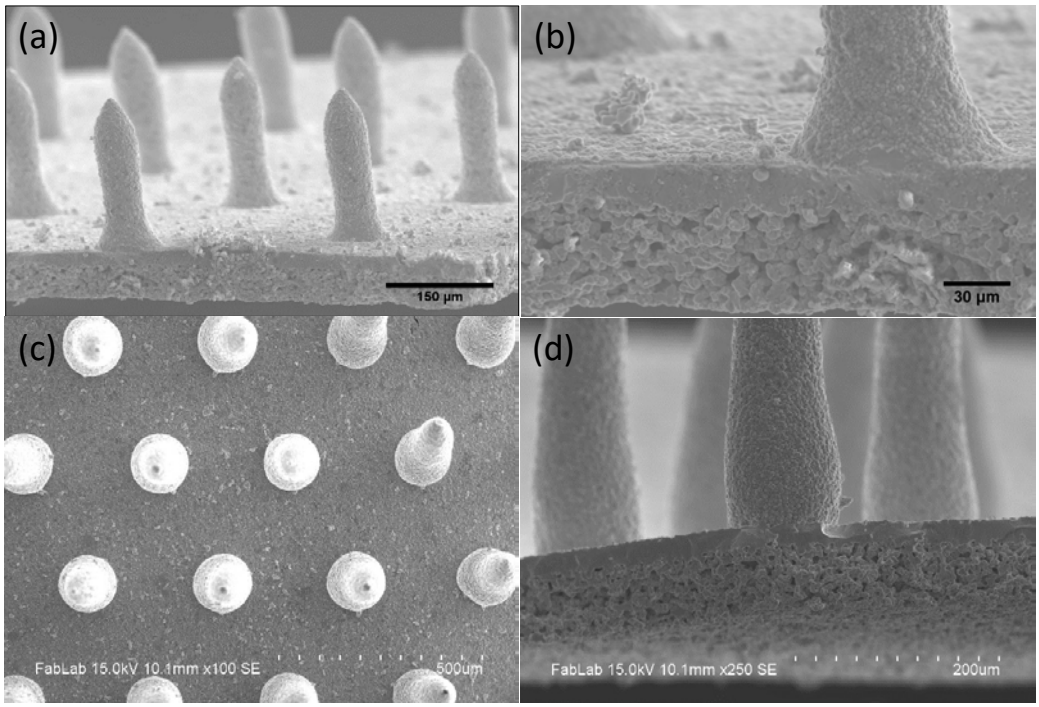

Figure 19. SEM images of 3D columns after sintering. The dense layer and the columns both sintered densely. (a) Zoom-out image and (b) Zoom-in image of the 3D-printed columns on a bilayer LLZ substrate with the column dimensions: 56-62 µm in diameter and 207-215 µm in height. (c) Top-down image and (d) cross-section/side-view of the 3D-printed columns on a bilayer LLZ substrate with the column dimensions: 350 µm height and 110 µm diameter.

Task 2: Develop and Validate Integrated Power and Energy Density Models

Milestone 2.1 Integrate power & energy density models to design optimized grid & column structures

Updates were made to the previous model to greatly improve its runtime efficiency. Using Finite Element Computational Software (FEniCS), the complexity of the model was reduced by converting the data points from a uniform voxel arrangement to a mesh of vertices. This change reduced the complexity of the model on average by 5X, reducing the runtime from hours to minutes. This increase in efficiency was imperative to the addition of other physical phenomena to the model, such as the tracking of additional phases of polysulfides, and the contributions of ohmic resistance and surface overpotentials. Meshes are superior compared to uniform voxels models when describing intricate, rounded structures because of their innate flexibility. Figure 20 is a column structure at a resolution of 30 pixels per axis. The mesh representation is much closer to that of the 3D printed structure and uses 1/6 the number of vertices as the voxel model (5,000 compared to 30,000).

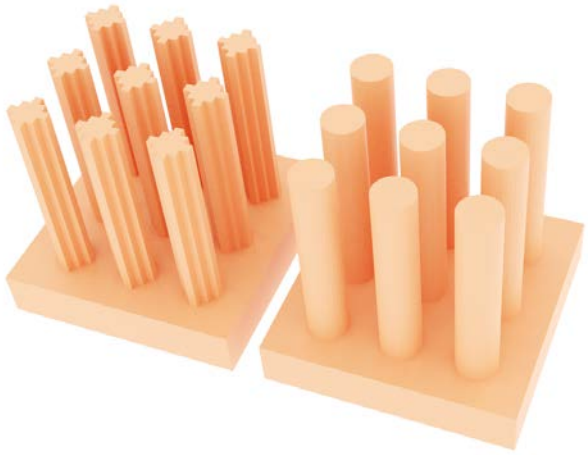

Figure 20. A comparison of the fidelity of voxel vs. mesh models. Mesh models (Right) are a much closer representation of the 3D printed structures and should yield more realistic results.

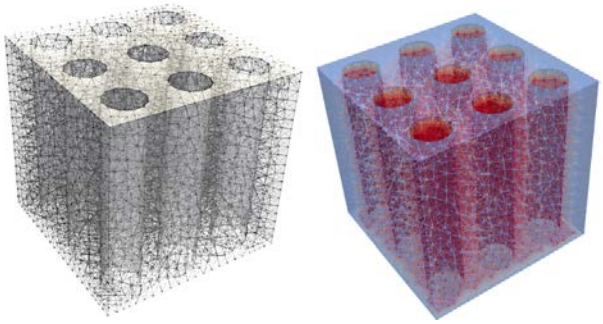

Figure 21. A depiction of the vertices and connections of the Finite Element Analysis mesh with a superimposed electrode structure (Left), and another image showing the diffusion of lithium throughout the mesh throughout the pillar structure (Right).

The equations governing the diffusion of lithium throughout the model needed to be altered to fit the format of the mathematical solver. By reducing the degree of differentiation through integration by parts, the new (but mathematically equivalent) equations can be quickly solved using FEniCS. Preliminary tests were run without the additional functionality of polysulfides or overpotentials. Figure 21 shows the network of vertices in the solid mesh and how they interact with each other while the simulation is running. The mesh's

calculations appear consistent with previous model iterations, as shown by the two cross-sections in Figure 22.

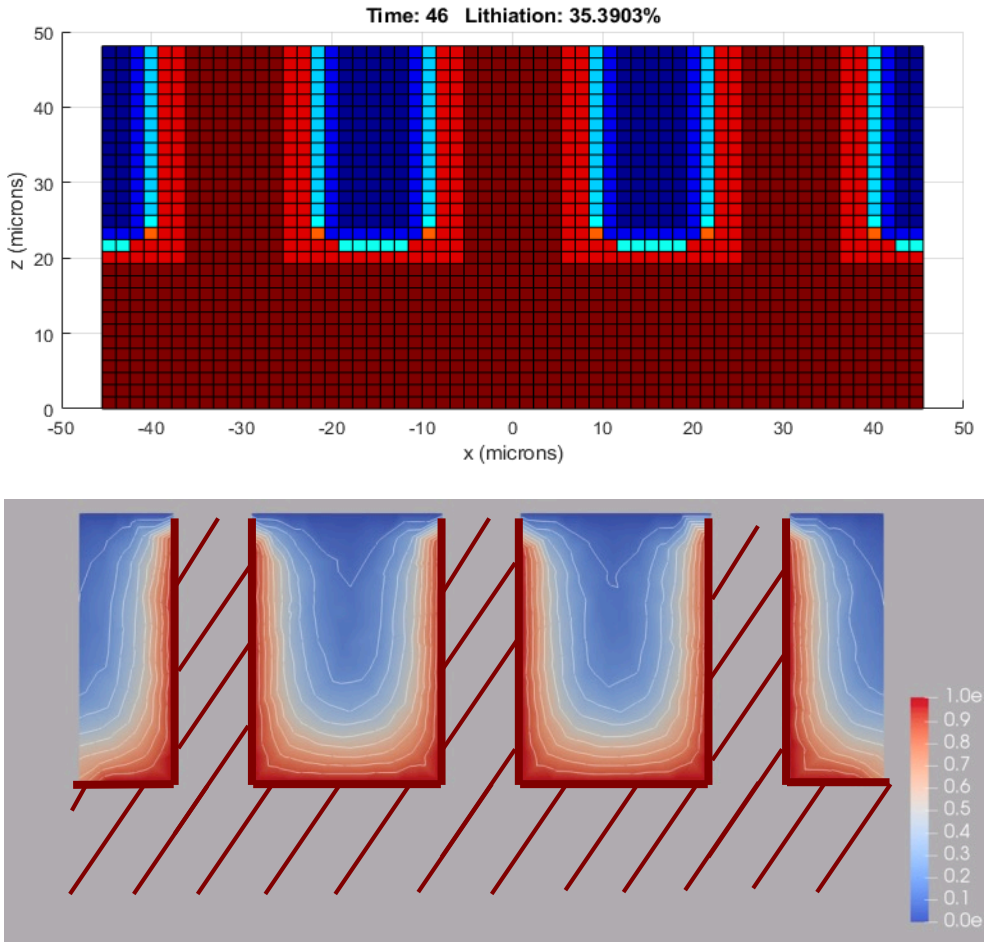

Figure 22. The calculated lithium concentration for the voxel-based model (top) vs mesh (bottom) visualized. Warmer regions indicate higher lithium concentration relative to its maximum concentration (Li_2S in this case).

The two figures in Figure 22 represents cross sections of the same physical system – 3D printed columns on top of the dense ionic separator. Both figures also use the same color map, with warmer indicating regions of higher lithium concentration relative to its maximum concentration (Li_2S for the electrode). The crossed out section in the Paraview plot (bottom figure) indicates regions of garnet electrolyte. The results from the meshed system are plainer to see and more accurate as vertices are not limited to the standard cardinal directions (a vertex can be connected to any number of other vertices anywhere on the mesh, but one voxel is only connected to its neighboring 6 voxels.)

When looking to optimize a cell's energy or power density by 3D printing, the variable constraints are the given geometry, the features' diameters and their separation. Assuming complete utilization of the electrode, energy density becomes a function solely of the electrode volume, or the porosity of the electrolyte. Changes were made to the previous model to implement the traditional vertex-based mesh framework of finite element analysis. Vertex-based representations are more advantageous when compared to voxel-based ones for two main reasons: computational efficiency and spatial fidelity. No changes were made to the underlying calculations or equations of the model.

Calculations were run to examine the effect of feature size on electrode utilization at a fixed porosity for column structures (Figure 23). The vertex-based calculations follow the same trend predicted by the voxel-based approach: smaller features more quickly utilize the electrode material, leading to higher power densities because the maximum distance that the lithium must diffuse to react with the cathode is reduced. The same results hold for the grid geometry as well. In comparing the grid to the column geometries with identical electrode volumes, the column geometry has a higher power density due to the higher total surface area.

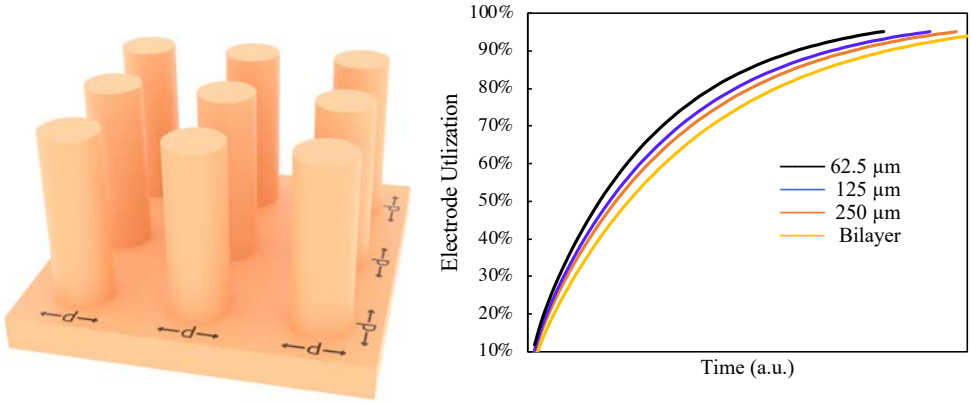

Figure 23. Percent utilization of the electrode material over time in different column geometries with fixed porosity. Decreasing feature size decreases the average distance lithium ions must travel to activate new electrode material. In a diffusion-limited system at a fixed porosity, this means that smaller feature sizes lead to faster and more complete electrode utilization.

Task 3: Optimization of Li-S Cells with Grid Cathode Garnet Structure

Milestone 3.1 Achieve an Li/SSE/S cell energy density of ≥300Wh/kg (Go-No Go is achieving ≥300Wh/kg with either Li/SSE/S or Li/SSE/NMC, Milestone 3.1 or 4.2, respectively)

To optimize the Li-S cell performance with grid cathode garnet structure, we compared multiple cells with various grid geometries. The initial impedance and cycling performance of these cells were measured for comparison. In these cells, a sulfur-carbon composite (S/C) was used as cathode and mixed with CS_2 to form slurries for infiltration into the grid structure. The total sulfur loading was 3 to 4 mg/cm^2. 30 µL liquid electrolyte was added to the cathode side to facilitate Li ion transport across cathode-electrolyte interface. Li metal was infiltrated into the anode garnet structure in molten form and then cooled down. The schematic structure of a full Li-S cell is shown in Figure 24a. From SEM images and EDX mapping in Figure 24b, it is seen that Li metal is well infiltrated into the porous layer of garnet electrolyte, and sulfur/carbon cathode is conformally coated on the printed-grid side.

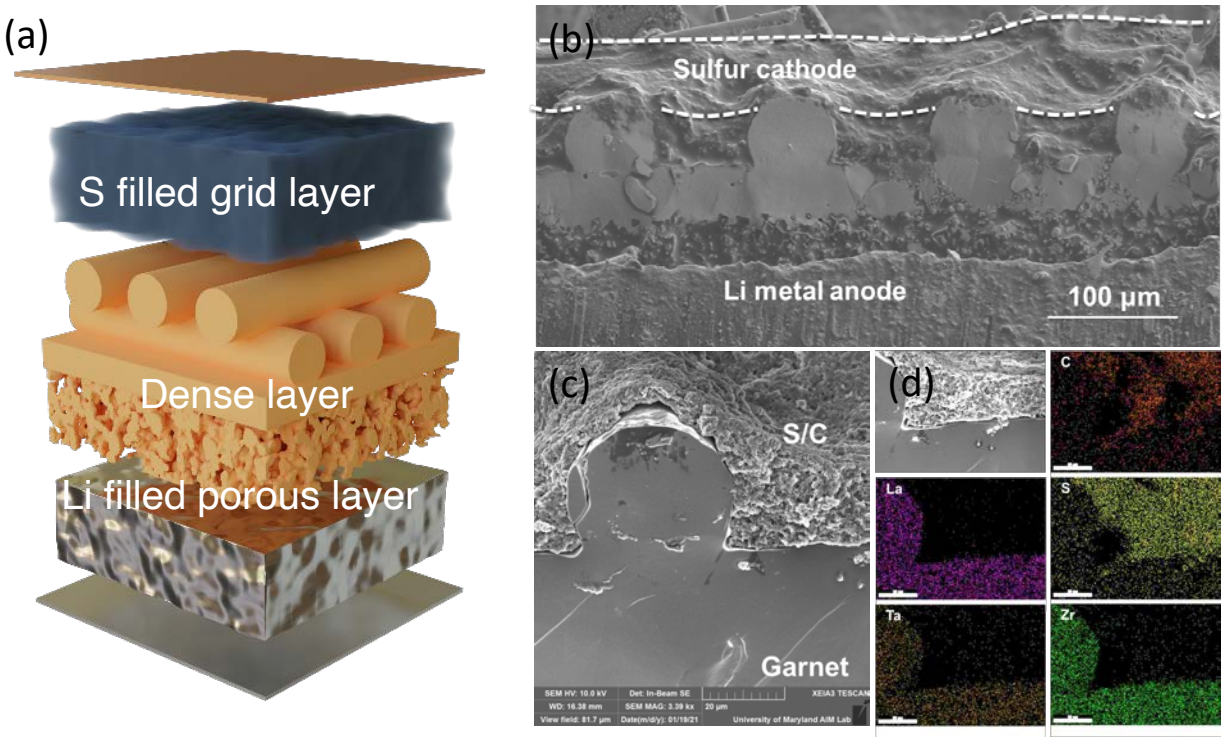

Figure 24. (a) Schematic structure of a Li|bilayer-grids electrolyte|S cell, (b, c) cross-sectional SEM of a typical cell and (d) the corresponding EDS mapping.

The cells were tested at room temperature. Three representative cell geometries and the cell performance are shown in Figure 25. A discharge capacity around 700-750 mAh/g was achieved in the first several cycles for all three cells (Figure 25d, h and l). However, cell 2 and 3 presented a gradual capacity decay in subsequent cycles while the capacity of cell 1 remained essentially unchanged. The results suggest that a self-supporting 3D printed grid structure helps decrease the cathode/electrolyte interfacial impedance (Figure 25c, g and k), improving the cycling stability of the cell. By summarizing the initial impedances of more cells, we have further found that the specific capacity increases with the decrease of area specific resistance of the cell (Figure 26), indicating a good bulk/interfacial ionic conductivity can improving the utilization of cathode active material.

Based on the above analysis, we further adjusted the grid geometry and have eventually achieved a close to theoretical discharge capacity for the first several cycles in a Li-S cell (Figure 27). The grid geometry of this cell is marked in the SEM images (Figure 27a and b). In addition to modifying the grid geometry, we also added a thin layer of PEO polymer electrolyte onto the grid structure to prevent the direct contact between the sulfur cathode and the garnet electrolyte. This strategy has proved to be critical in achieving high utilization of sulfur cathode (see later discussion).

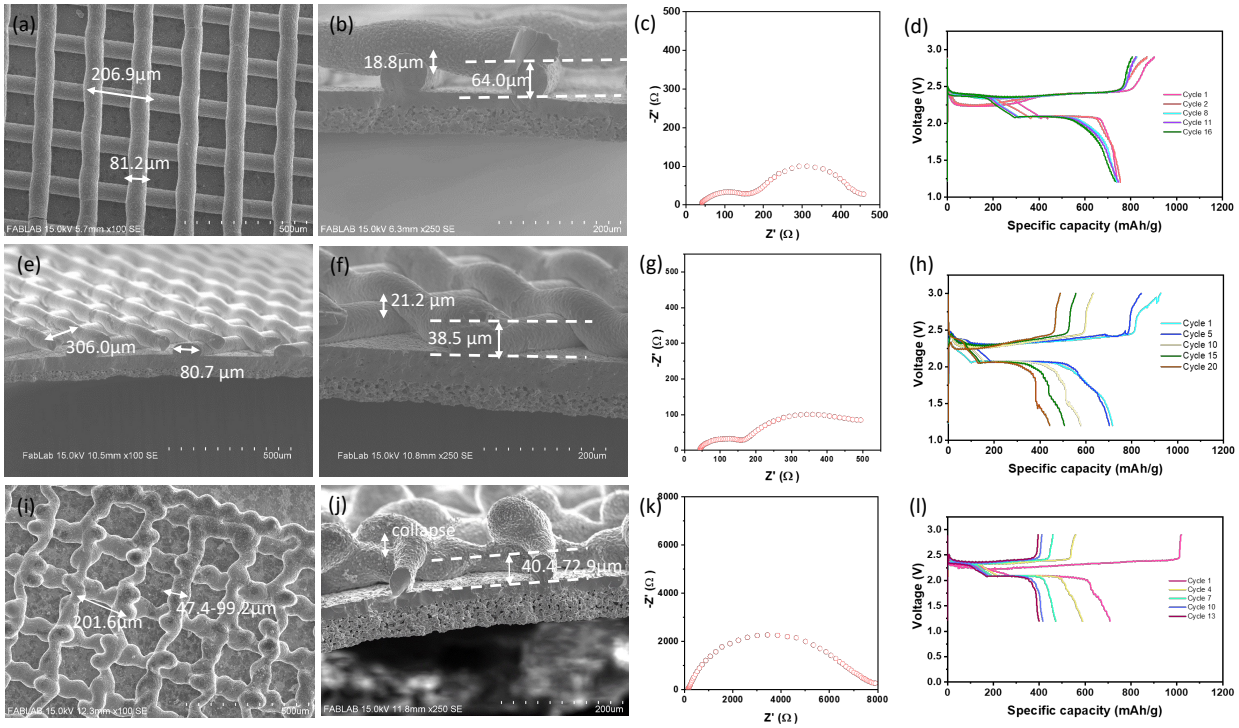

Figure 25. Cell 1: (a, b) SEM images of the grid structure, (c) initial impedance and (d) charging and discharging curves for different cycles. Cell 2: (e, f) SEM images of the grid structure, (g) initial impedance and (h) charging and discharging curves for different cycles. Cell 3: (i, j) SEM images of the grid structure, (k) initial impedance and (l) charging and discharging curves for different cycles.

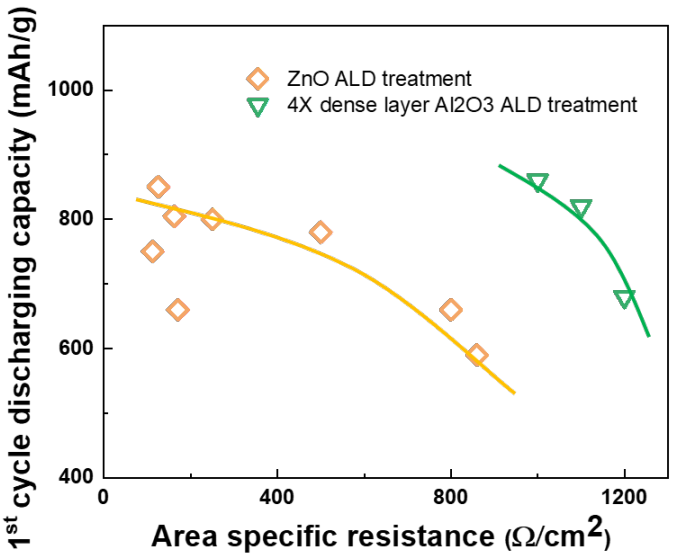

Figure 26. The relation of 1st cycle discharge capacity vs. area specific resistance for multiple Li-S cells with grid garnet structure and either ZnO or Al_2O_3 as the interlayer for improving Li/dense garnet layer interface. The solid lines are a guide to the eye.

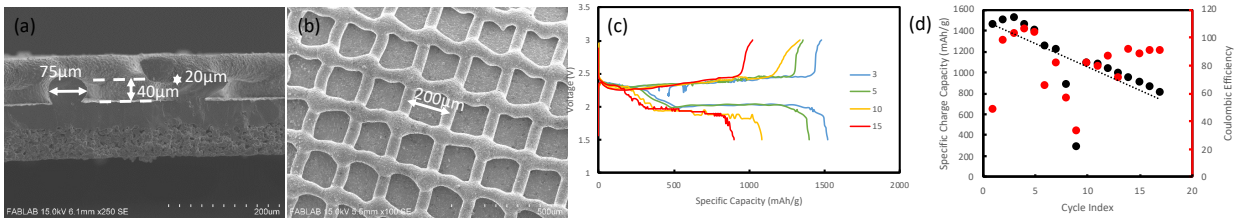

Figure 27. Cell4: (a, b) SEM images of the grid structure, (c) charging and discharging curves for different cycles and (d) specific capacity and coulombic efficiency variation with cycle number.

To rationally predict the performance of the cell with the same structure as cells 1, 2 and 4 (the geometry of cell 3 is too irregular to be modeled), we modified the cell design model developed in Task 2 according to the real geometries and impedances of the cells. The curves of the specific capacity vs. C-rate were then calculated from these modified models and validated by comparison with the experimental results (Figure 28). Only cell 4 exhibited the same specific capacity as predicted by the model while cell 1 and cell 2 exhibited specific capacities significantly lower than predicted. This indicates the possible reaction between sulfur cathode and the garnet electrolyte, which can be prevented by a thin PEO polymer coating between the two components. With respect to the effect of 3D grid geometry on the cell performance, comparison between different modeling curves suggests that the conformal grid structure cycles better at higher C-rates because of the low tortuosity and constriction penalties to effective conductivity and self-supporting grid performs better at lower C-rates because of the increased surface area and increased access to active material farther from the separator. The newest structure in cell 4 is predicted to enable higher capacities across all C-rates because of the decreased first layer height; bringing the second layer closer to the separator allows it to function more effectively to extend cathode thickness.

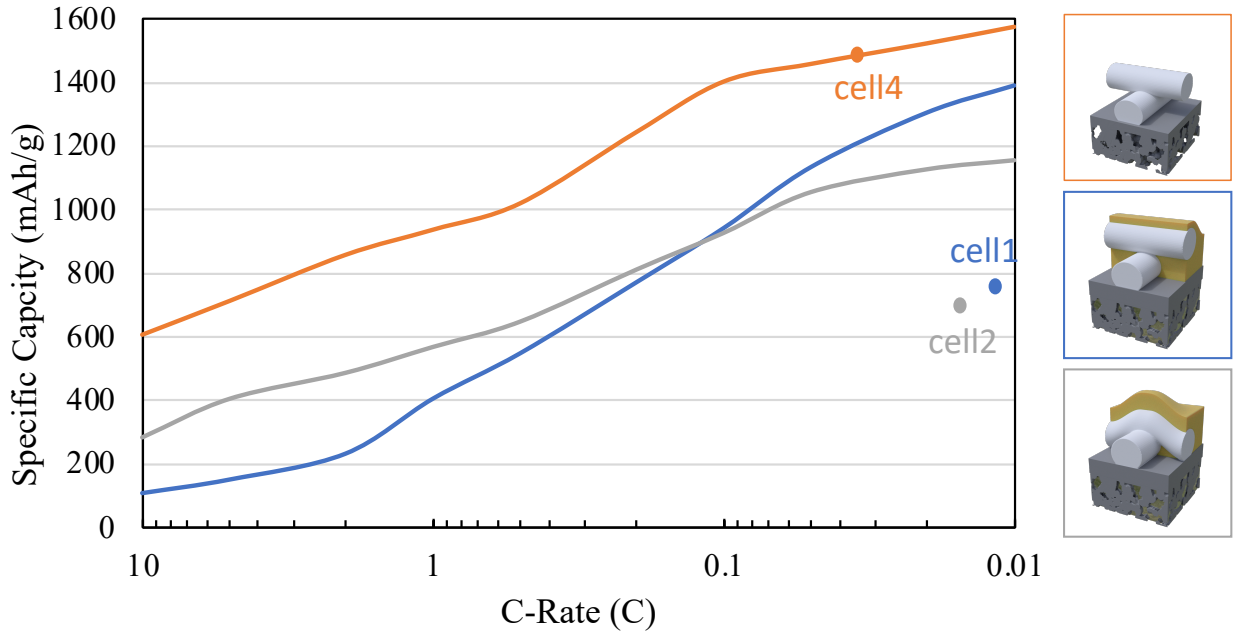

Figure 28. The simulated curves of the specific capacity vs. C-rate for the Li-S cells with the same grid geometry as cells 1, 2 and 4. The dots represent the experimental data points of these cells. The 3D schematics of the cell geometries are shown in the right-side column.

Task 4: Optimization of Li-NMC Cells with Column Cathode Garnet Structure

Milestone 4.1 Down-select "Li-free" anode structure (Cu-coated vs. carbon-filled porous garnet).

Table 1. Comparison of CNT and Cu current collector

Cell with current collector type	CNT carbon	Sputtered Cu
Morphology	Conformal with the porous structure	A thin layer on the surface of porous layer
Impedance	Low and consistent	High initially, decreased after cycling
Cycling stability	High, owing to the conformal structure	Relatively low due to the formation of Li particles away from Cu
Fabrication simplicity	simple	Complex, with risk of exposure to air
High current density feasibility	Have demonstrated 1 mA/cm^2 (Ref.: Nano Lett. 2018, 18, 3926-3933)	Have demonstrated 0.5 mA/cm^2 (Ref.: PNAS, 2018, 115, 3770-3775)

We have experimentally considered different aspects for two "Li-free" anode structures, conformal carbon (carbon nanotube, CNT) coating internal to the garnet anode pores and an external Cu current collector, and summarized that an infiltrated CNT is more favorable. Table 1 lists the properties we have investigated to compare the two different approaches, together with the detailed experiments to support our choices. To compare the two different approaches, we employed garnet bilayers to assemble Li | garnet | carbon, and Li | garnet | copper cells to carry out Li stripping and plating test. The bilayer was synthesized via tape casting approach with a typical 30 μm dense layer and 60 μm porous layer (Figure 29).

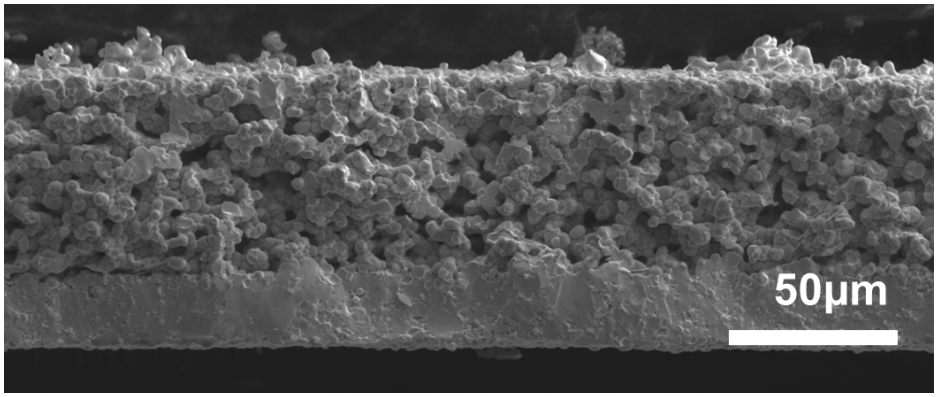

Figure 29. SEM of cross-sectional bilayer with dense-porous structure.

The schematic structure of the cells with carbon and copper can be seen in Figure 30 and Figure 31. The mechanisms of Li plating on the porous sides are different. For the internal carbon, CNTs are uniformly coated into the pores on the porous side of the bilayer structure, introducing electronic conductivity on the surface of garnet electrolyte within the framework (Figure 30). With the ionic conductivity provided by the SSE, lithium ions flow in the garnet electrolyte while electrons flow along the CNTs at the surface, thus forming a mixed electron/ion conducting framework.

For the external copper current collector deposited on the surface of porous side, Li is plated from the bottom (outside the pore structure) and rises during deposition, away from the separator layer and free from electrolyte penetration and short circuit (Figure 31). Owing to the solid-state deposition property, Li grows smoothly in the pores of the garnet host without forming Li dendrites.

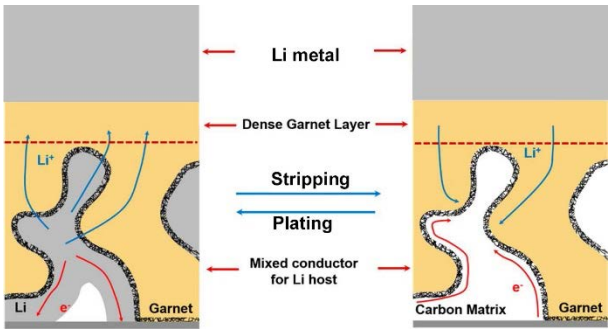

Figure 30. Schematic demonstrating the working principle of the CNT carbon current collector for bilayer garnet.

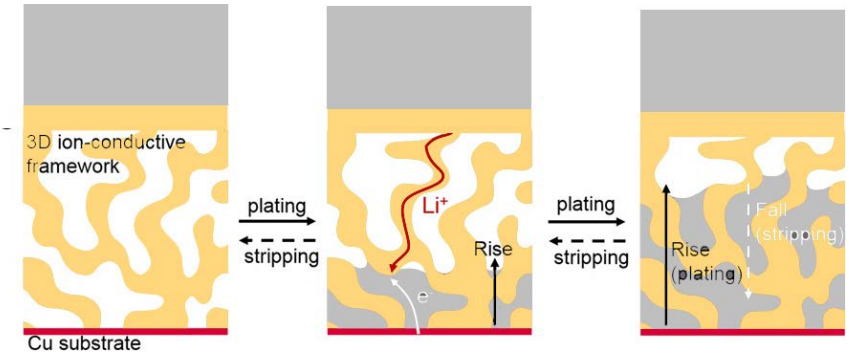

Figure 31. Schematic demonstrating the working principle of the copper current collector for bilayer garnet.

For the counter electrode, Li metal was heated to melt on the dense side of bilayers. Due to the atomic layer deposition (ALD) treatment, good interface between Li metal and dense garnet layer can be achieved (Figure 32).

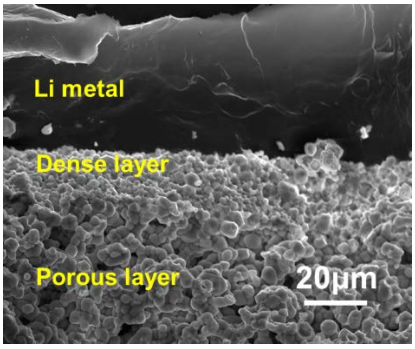

Figure 32. Good interface between Li metal and dense layer was achieved.

For the internal carbon, CNT was dispersed in dimethylformamide (DMF) to form a CNT ink (1 mg/mL) and infiltrated repeatedly into the porous layer of the bilayer garnet until the surface was completely black. This CNT ink approach is scalable (Figure 33a). The external Cu current collector was sputtered on the surface of the porous layer with a thickness of 400 nm by electron-beam physical vapor deposition on an Angstrom NexDep Ebeam Evaporator (Figure 33b and c).

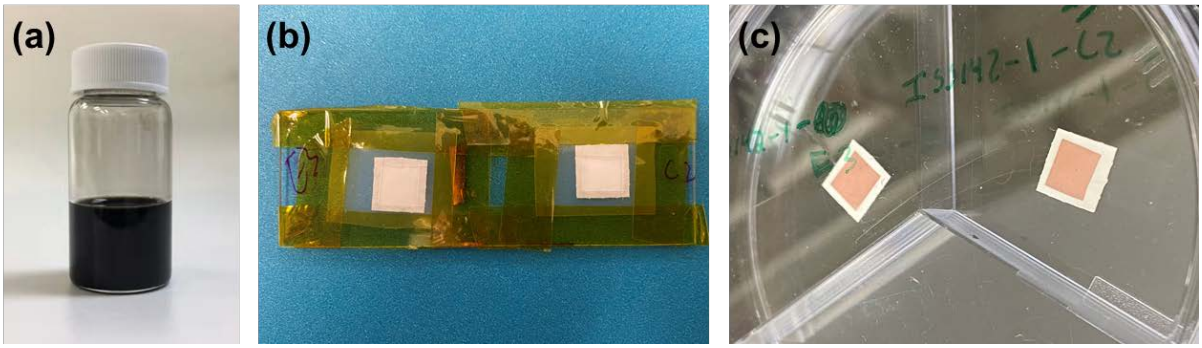

Figure 33. (a)CNT ink, which indicates good scalability. Bilayer garnet (b) before and (c) after Cu sputtering.

The Li-Garnet-CNT cell was assembled as shown in Figure 34a. The Li metal counter electrode was melted on the dense side of the bilayer, while the CNT current collector was infiltrated into the porous layer. The as-assembled cell was pre-cycled with current density 0.01 mA/cm^2 and 0.02 mA/cm^2 for 10 cycles respectively to improve the interface between Li-metal and garnet electrolyte. Figure 34b and c presents the impedance change before and after pre-cycling. The impedance is somewhat decreased, indicating an improved interface. Figure 34d illustrates the Li plating and stripping cycles with current density 0.05 mA/cm^2. The negative potential indicates plating process (Li ions transport from the Li metal counter electrode on the dense layer side to the CNT porous side) and positive potential indicates stripping process (Li stripped from the CNT porous side back to the dense layer side). The cycling profile is stable for the tested 300 hours.

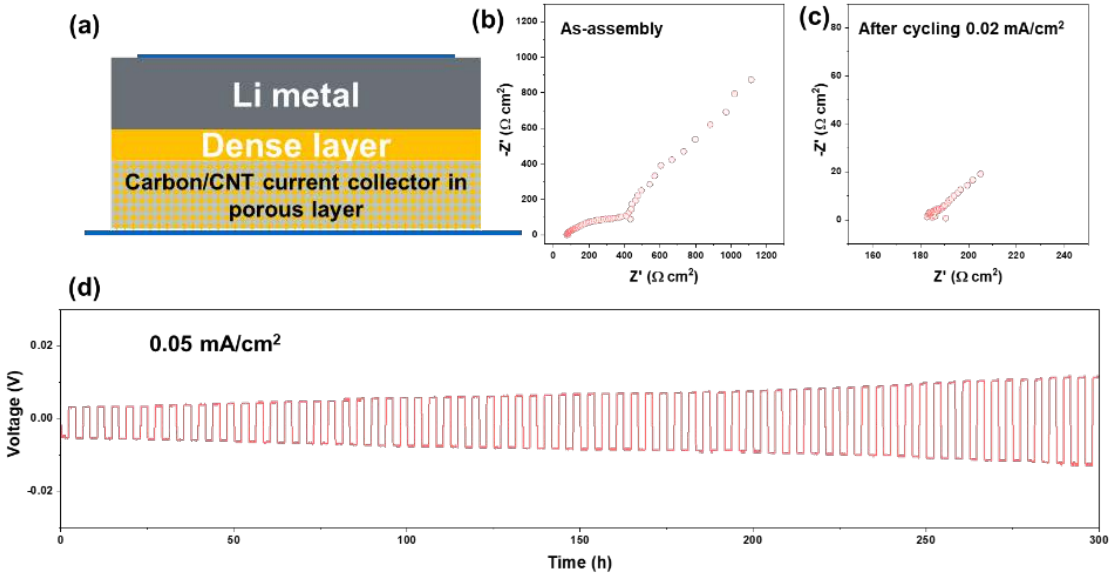

Figure 34. (a) Schematics of Li-Garnet-CNT cell. (b) EIS of the as-assembled Li-Garnet-CNT cell (b) EIS of the as-assembled Li-Garnet-CNT cell after 0.02 mA/cm2, the impedance decreased slightly. (c) Li plating (negative potential) and stripping (positive potential) profile of the Li-Garnet-CNT cell.

It is noted that the polarization increased slightly with the cycling numbers. This should be attributed to the weakened interface between Li metal counter electrode and dense layer. The zoomed-in cycling profile in Figure 35a shows that the polarization resistance during plating is slightly larger in magnitude than stripping after long time cycles, which indicates it is harder to transport Li ions from the dense side. Post-mortem test was carried out. SEM images shows the formation of gaps between the Li metal counter electrode and the dense garnet layer, which can explain the continuous increase of polarization (Figure 35b and c). These

strongly indicates that the flat dense pellet structure is not optimal to maintain a good interface. To solve these issues, porous structures on both sides (trilayer) and CNT buffering are suggested.

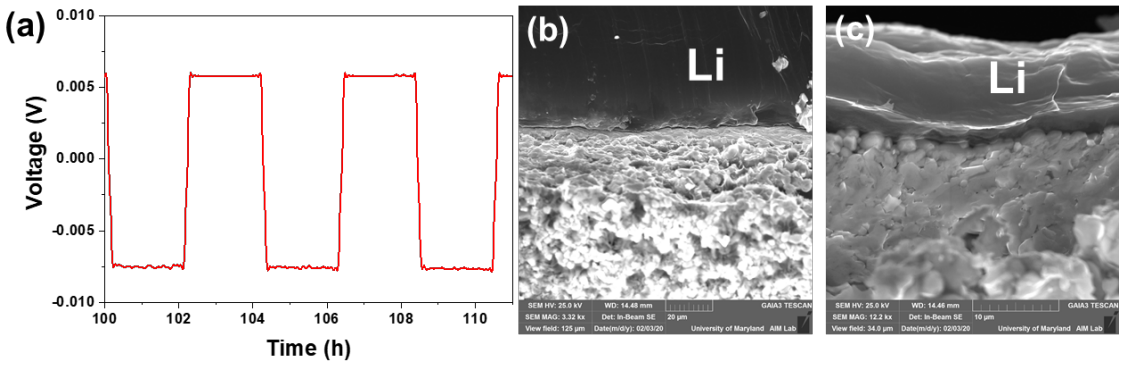

Figure 35. (a) Zoom-in cycling profiles for cell during 100 to 111 h. (b) and (c) SEM image of interface between Li metal and dense layer. Clear gaps can be seen after long time cycling.

The Li-garnet-Cu cell was assembled, whose structure is shown in Figure 36a. Li metal counter electrode was melted on the dense side of the bilayer, while the Cu current collector was sputtered on the surface of the porous layer. The as-assembled cell was pre-cycled with current density 0.01 mA/cm^2 and 0.02 mA/cm^2 for 10 cycles respectively to improve the interface between Li-metal and garnet electrolyte. Figure 36b and c presents the impedance change before and after pre-cycling. The impedance for initial cell is very large compared with the cell using CNT current collector. After pre-cycling treatment, the impedance is significantly decreased. However, it is noted that the impedance for external Cu cell is still larger than the cell with internal CNT. The conformal CNT coating infiltrated inside the porous layer can help decrease the impedance.

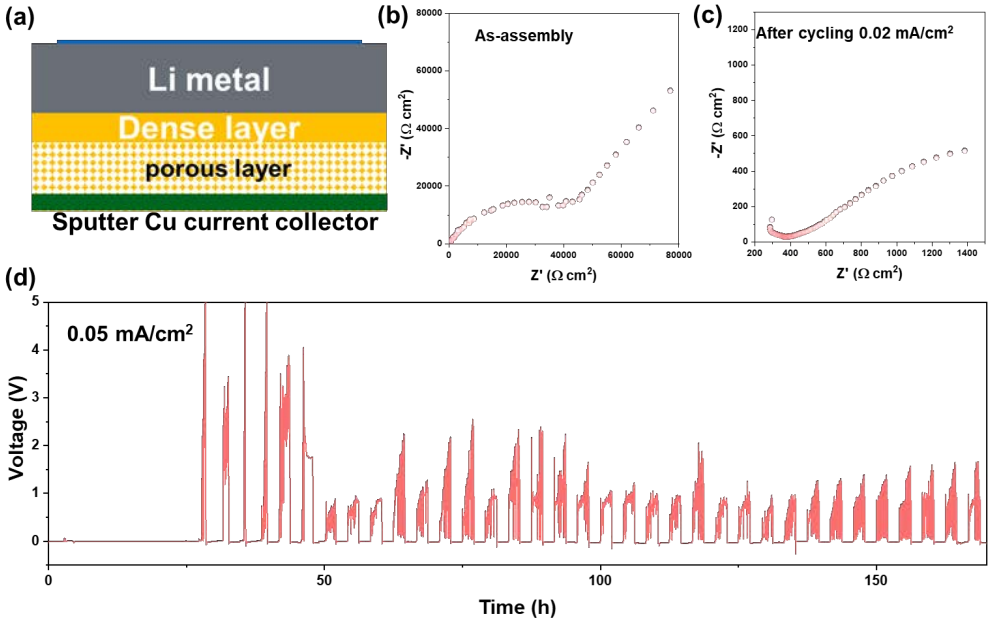

Figure 36. (a) Schematics of Li-garnet-Cu cell. (b) EIS of the as-assembled Li-Garnet-Cu cell (c) EIS of the as-assembled Li-Garnet-Cu cell after 0.02 mA/cm2. (d) Li plating (negative potential) and stripping (positive potential) profile of the Li-garnet-Cu cell.

Figure 36d presents the cycling profile of the cell with Cu current collector at a current density of 0.05 mA/cm^2. The polarization during the stripping process is very high. Post-mortem test revealed that during

plating process, Li metal can penetrate Cu current collector and form Li particles outside the Cu layer, resulting in a high impedance when going back during stripping (Figure 37).

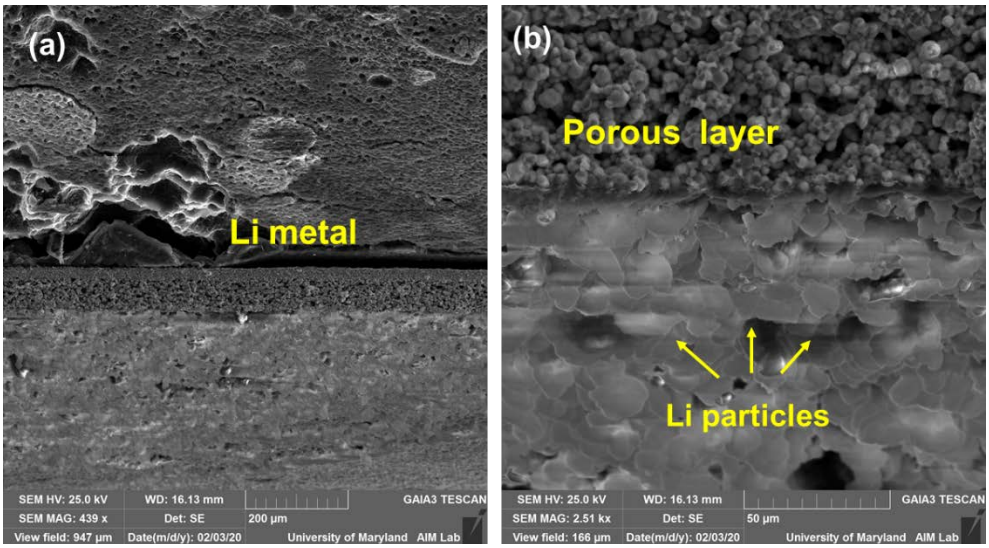

Figure 37. SEM images of the Li-garnet-Cu cell after plating/stripping. Li particles can be observed outside the sputtered Cu current collector, which can explain the high polarization when Li is being stripped back from the porous side to the dense side.

Our previous trilayer experiments showed that the cell with CNT current collector can reach a high current density of 1 mA/cm^2, whereas the cell with Cu current collector only reached 0.5 mA/cm^2 (Figure 38).

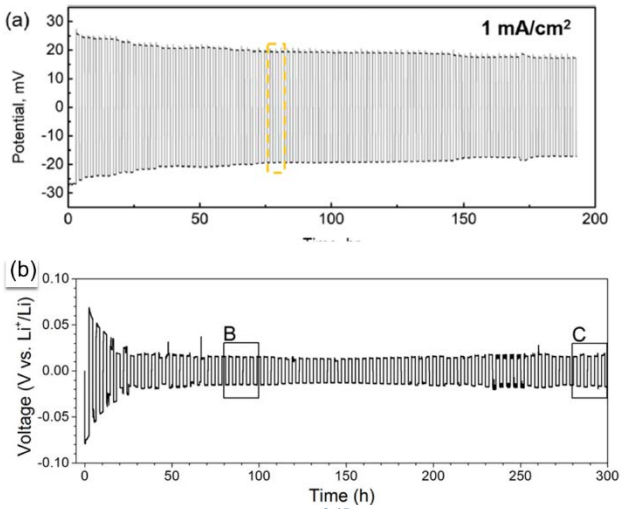

Figure 38. (a) Cycling for cell with CNT current collector at 1 mA/cm^2,[15] (b) Cycling for cell with Cu current collector at 0.5 mA/cm^2.[16]

Down select between the CNT and Cu current collectors

Based on the above data, the cell with infiltrated CNT presented lower initial impedance compared to the Cu current collector. The cell with the CNT presented better cycling stability with less polarization during Li plating and stripping. The CNT also showed better fabrication simplicity, as it only needs to infiltrate CNT ink and drying process, whereas for Cu current collector, template should be prepared and the garnet exposed to air, which is not good for cycling. Finally, the cell with the CNT has demonstrated a high current density of 1 mA/cm^2, whereas the cell with Cu current collector has demonstrated 0.5 mA/cm^2. In conclusion, internal carbon coating is the down selected choice from the two candidates based on our experimental data such as initial impedance, cycling stability, fabrication simplicity and high current density feasibility.

Milestone 4.2 Achieve an Li/SSE/NMC cell energy density of ≥300Wh/kg (Go-No Go is achieving ≥300Wh/kg with either Li/SSE/S or Li/SSE/NMC, Milestone 3.1 or 4.2, respectively).

To optimize the Li-NMC cell performance with column cathode garnet structure, we compared multiple cells with various column geometries. In these cells, the composite cathode comprising of NMC622 particles, carbon black and PVDF binder was applied onto the 3D-printed columns. The total NMC loading was 1 to 2 mg/cm^2. Minimum amount of liquid electrolyte was added to the cathode side to facilitate Li ion transport across cathode-electrolyte interface. The anode was based on Li metal infiltrated into the porous layer with ALD ZnO coating. The overall schematic structure of a Li-NMC cell is shown in Figure 39. Uniform coating of NMC powders on the column structure and intimate attachment of Li on the back side are confirmed by SEM (Figure 39b and c). Figure 39c-e shows various column geometries investigated in our study.

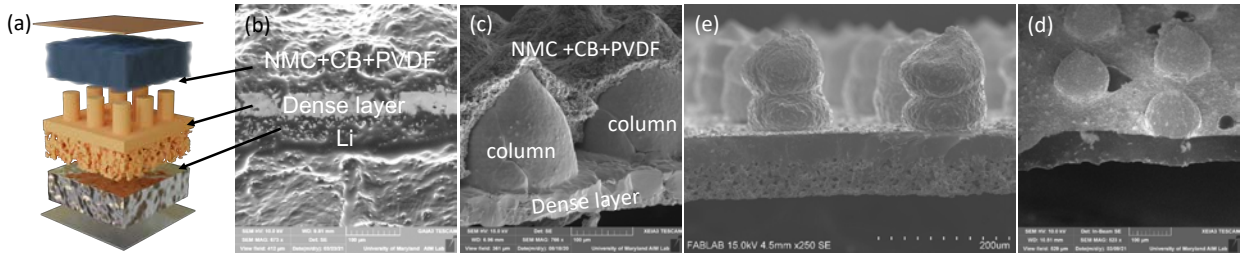

Figure 39. (a) Schematic structure of a Li|bilayer-column electrolyte|NMC cell, (b) cross-sectional SEM of a typical cell and (c-e) cross-sectional SEM of various column geometries on the bilayer electrolyte.

The cells were tested at room temperature. Figure 40a, b and c show the representative cell cycling performance corresponding to the column geometries shown in Figure 39c, d and e, respectively. The discharge and charge plateaus can be observed for all the cells, indicating normal cathode operation. Generally, as the column height decreases from 210 to 80 μm, the overpotential of the cell decreases and the capacity increases.

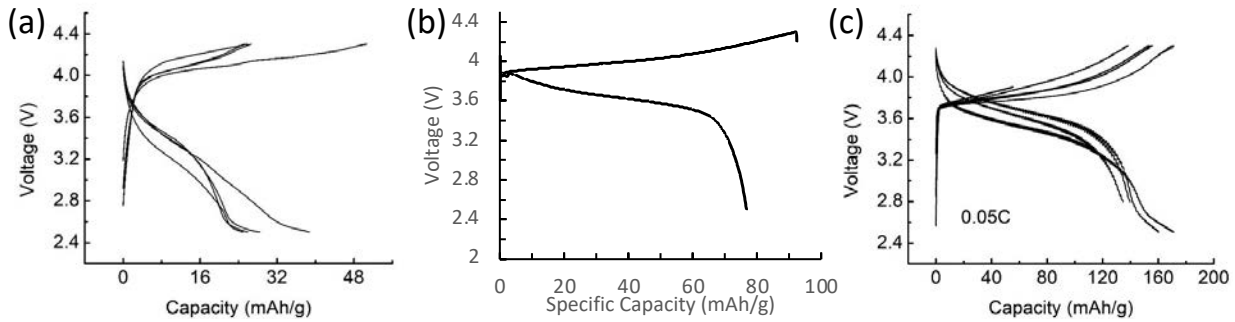

Figure 40. Charging and discharging curves for different cycles for the Li alloy||bilayer-column||NMC cells with column geometries shown in Figure 39c-e.

By comparing the cells with the same column height, we found that the capacity is more essentially governed by the cell resistance (cells 2-4 in Figure 41); lower overall cell resistance leads to higher accessible cathode thickness corresponding to higher capacity. The variation of the cell resistance for nominally the same column height is due to minor improvement in processing and subsequent actual column geometry. Figure 41 also includes a cell with taller columns (cell 1), which is consistent with the trend. Moreover, by reducing the cell resistance, we have been able to utilize the NMC thickness in the same range as the commercial calendared cathode. This is a critical improvement for solid-state batteries that may not be able to accommodate calendared cathodes due to manufacturing constraints imposed by the more brittle nature of the solid electrolyte.

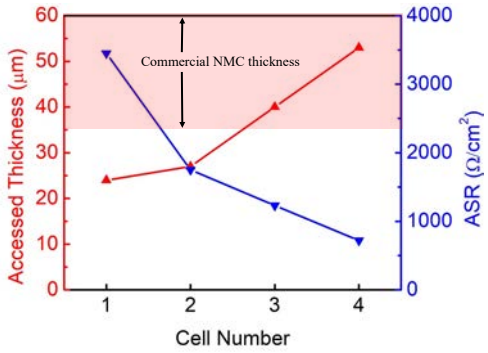

Figure 41. Comparison between four Li alloy||bilayer-column||NMC cells to reveal the relationship between the overall cell areal specific resistance and the accessible NMC cathode thickness. The accessible NMC cathode thickness is calculated based on the cell capacity and assuming achievable specific capacity of 180 mAh/g for NMC.

To rationally evaluate the performance of the cells demonstrated in Figure 40, we modified the cell design model developed in Task 2 according to the real column geometries and impedances of the cells. The curves of the specific capacity vs. C-rate were then calculated from these modified models and validated by comparison with the experimental results (Figure 42). Comparison between the experimental result and the modeling result indicates that shorter columns can enable the full utilization of the cathode active material while taller columns are more likely to cause poor contact and worse performance from NMC detaching at the interface. Using the validated model, we have further predicted an improved column geometry that can enable a higher cell performance (yellow curve in Figure 42). Expectantly, the new geometry can improve the cell rate performance once developed.

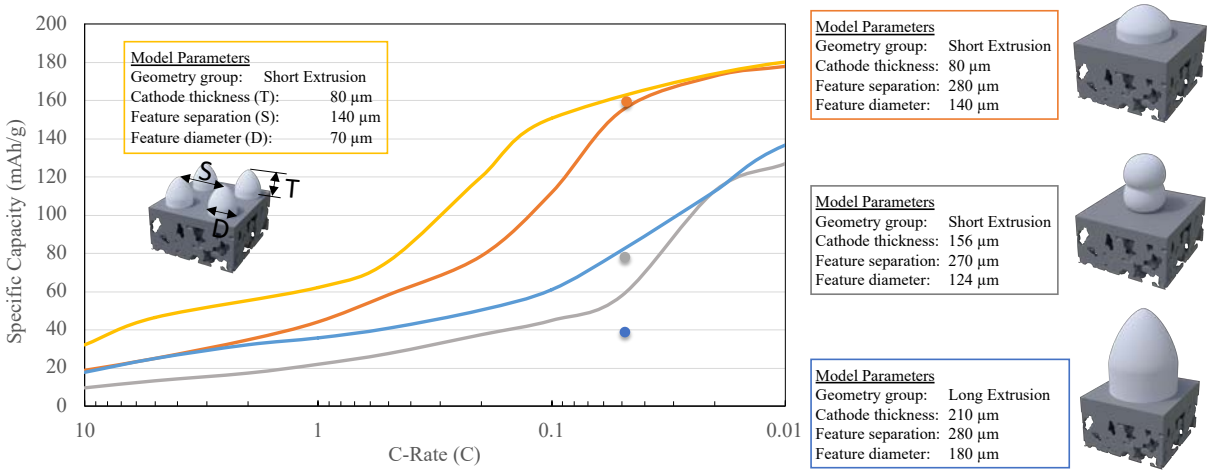

Figure 42. The simulated curves of the specific capacity vs. C-rate for the Li||bilayer-column||NMC cells with the column geometries illustrated inside and on the right of the plot. The dots represent the experimental data points of the actual cells with the same column geometries, i.e., the cells demonstrated in Figure 39.

Based on the validated model, we imagined four column geometries and calculated the specific energy as a function of C-rate for the corresponding Li-NMC cells (Figure 43). We found: (1) S-shape correlation between C-rate and specific energy; (2) the cells with decreased printed feature dimensions (feature diameter and inter-feature separation) can achieve higher specific energy at a given C-rate; (3) the 500 Wh/kg goal is achievable for Li-NMC cells with technically practical column geometries. Hence, we have developed the first solid-state battery performance model to provide critical design criteria for achieving 500 Wh/kg energy goal as function of C-rate.

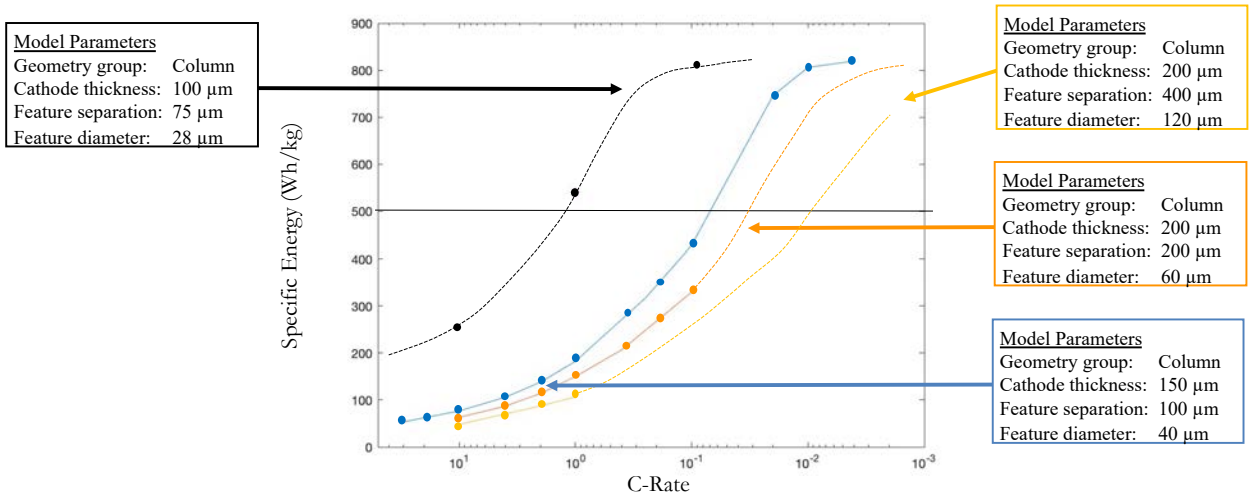

Figure 43. The simulated curves of the specific energy vs. C-rate for the Li||bilayer-column||NMC cells with various column geometries.

Task 5: Scale-Up Cell Size and Deliver ≥500 Wh/kg Cells for Independent Testing

Due to the impact of COVID 19 limiting access to necessary laboratories cell fabrication and testing was severely impeded and sufficient progress on this task was unfortunately not achieved before end of project.

Summary

Fabricated controlled 3D porous SSE structures by 3D printing - Methods were developed to control the 3D-printing garnet ink rheological properties. By carefully controlling rheology and drying rates, the ink properties were tuned to print different structures, including columns and multilayer grid structures of varying dimensions directly on garnet substrates. Column structures were printed with 56-180 µm diameters, 50-210 µm heights and 237-333 µm separations, providing 37-94% layer porosities. Multilayer grid structures were printed with 50-150 µm line diameters and 140-350 µm line spacing, providing 60-70% layer porosities. Both structures provide direct Li^+ transport pathways, additional electrode/electrolyte interfacial area, and designs to increase mechanical strength.

Developed 3D solid-state ionic and electronic transport models - Models were developed to compare the performance of different 3D printed electrolyte structures with varied geometries, feature diameters and separations, thus using material properties it was possible to determine effect of structure on Li^+ and electron transport by mapping the movement of Li^+ through the cathode over time through an iteratively using the Nernst-Planck equation. By applying the model to varied 3D-printed feature dimensions, the effect of geometry was resolved by trends in electrode utilization and ion flow, enabling design optimization of 3D-printed SSE structures to maximize cell energy and power density, with following major conclusions: (1) energy density is directly related to a structure's porosity and thus electrode loading, which is a function of feature diameter, separation, and height; (2) structures with smaller SSE feature diameters and thus spacing have higher power density because the maximum distance that Li must flow to react with electrode material is decreased; (3) column structures have improved ion/electron transport rates compared to grid structures, albeit with lower mechanical strength; and (4) grid structure electrochemical performance can be improved by staggered overlapping layers.

These cell design models were modified in Phase 2 according to the real geometries and impedances of the cells to rationally evaluate the performance of the cells and compared with the experimental results. The comparison results suggest that: the conformal grid structure cycles better at higher C-rates because of the low tortuosity and constriction penalties to effective conductivity and self-supporting grid performs better at lower C-rates because of the increased surface area and increased access to active material farther from the separator; shorter columns can enable the full utilization of the cathode active material while taller columns are more likely to cause poor contact and worse performance from NMC detaching at the interface.

Down-selected CNTs coated porous garnet as a preferred "Li-free" anode structure - garnet bilayers were employed to assemble Li | garnet | carbon and Li | garnet | copper cells to carry out Li stripping and plating test. The CNT coated anode pores showed better fabrication simplicity, as it only needs to infiltrate CNT ink and drying process, whereas for Cu current collector, template should be prepared and the garnet exposed to air, which is not good for cycling. Compared to the Cu current collector, the cell with CNT presented lower initial impedance and better cycling stability with less polarization during Li plating and stripping. Previous research shows that the cell with the CNT current collector has demonstrated a high current density of 1 mA/cm^2, whereas the cell with Cu current collector has demonstrated 0.5 mA/cm^2. Therefore, carbon coated anode pores were down selected as the most favorable "Li-free" anode structure.

Demonstrated application of 3D-printed garnet structures in full cells - full cells using sulfur cathode on 2-layer garnet grids structure or NMC cathode on garnet column structure were fabricated. By adjusting the geometry of the 3D-printed structure, the Li-S cell cycling at C/33 and Li-NMC cell cycling at C/20 achieved near theoretical discharge capacities of 1450 mAh/g and 170 mAh/g, respectively. In particular, with our 3D cathode structures we were able to achieve these discharge capacities without benefit of cathode calendaring which is intrinsically difficult for garnet solid electrolytes.

Moreover, it should also be pointed out that the experimentally validated cell structure/performance models provided the critical design criteria for Li-NMC and Li-S cells to achieve >500 Wh/kg energy goal as function of C-rate. Thus, indicating with additional experimental effort these goals are achievable with our 3D printed structures.

Acknowledgement

This material is based upon work supported by the U.S. Department of Energy's Office of Energy Efficiency and Renewable Energy (EERE) as part of the Battery 500 Consortium, Award Number DE-EE008201.

Reference

(1) Bruce, P. G.; Freunberger, S. A.; Hardwick, L. J.; Tarascon, J.-M. Li-O_2 and Li-S batteries with high energy storage. *Nat. Mater.* **2012,** *11* (1), 19.
(2) Xu, K. Electrolytes and Interphases in Li-Ion Batteries and Beyond. *Chem. Rev.* **2014,** *114* (23), 11503.
(3) Quartarone, E.; Mustarelli, P. Electrolytes for solid-state lithium rechargeable batteries: recent advances and perspectives. *Chem. Soc. Rev.* **2011,** *40* (5), 2525.
(4) Takada, K. Progress and prospective of solid-state lithium batteries. *Acta Mater.* **2013,** *61* (3), 759.
(5) Thangadurai, V.; Narayanan, S.; Pinzaru, D. Garnet-type solid-state fast Li ion conductors for Li batteries: critical review. *Chem. Soc. Rev.* **2014,** *43* (13), 4714.

(6) Luntz, A. C.; Voss, J.; Reuter, K. Interfacial Challenges in Solid-State Li Ion Batteries. *The Journal of Physical Chemistry Letters* **2015,** *6* (22), 4599.
(7) Wang, Y.; Richards, W. D.; Ong, S. P.; Miara, L. J.; Kim, J. C.; Mo, Y.; Ceder, G. Design principles for solid-state lithium superionic conductors. *Nat. Mater.* **2015,** *14* (10), 1026.
(8) Gadjourova, Z.; Andreev, Y. G.; Tunstall, D. P.; Bruce, P. G. Ionic conductivity in crystalline polymer electrolytes. *Nature* **2001,** *412* (6846), 520.
(9) Christie, A. M.; Lilley, S. J.; Staunton, E.; Andreev, Y. G.; Bruce, P. G. Increasing the conductivity of crystalline polymer electrolytes. *Nature* **2005,** *433* (7021), 50.
(10) Aetukuri, N. B.; Kitajima, S.; Jung, E.; Thompson, L. E.; Virwani, K.; Reich, M.-L.; Kunze, M.; Schneider, M.; Schmidbauer, W.; Wilcke, W. W.et al. Flexible Ion-Conducting Composite Membranes for Lithium Batteries. *Advanced Energy Materials* **2015,** *5* (14), 1500265.
(11) Zhou, D.; He, Y.-B.; Liu, R.; Liu, M.; Du, H.; Li, B.; Cai, Q.; Yang, Q.-H.; Kang, F. In Situ Synthesis of a Hierarchical All-Solid-State Electrolyte Based on Nitrile Materials for High-Performance Lithium-Ion Batteries. *Advanced Energy Materials* **2015,** *5* (15), 1500353.
(12) Pan, Q.; Smith, D. M.; Qi, H.; Wang, S.; Li, C. Y. Hybrid Electrolytes with Controlled Network Structures for Lithium Metal Batteries. *Adv. Mater.* **2015,** *27* (39), 5995.
(13) Fu, K.; Gong, Y.; Dai, J.; Gong, A.; Han, X.; Yao, Y.; Wang, C.; Wang, Y.; Chen, Y.; Yan, C.et al. Flexible, solid-state, ion-conducting membrane with 3D garnet nanofiber networks for lithium batteries. *Proceedings of the National Academy of Sciences* **2016,** *113* (26), 7094.
(14) Hitz, G. T.; McOwen, D. W.; Zhang, L.; Ma, Z.; Fu, Z.; Wen, Y.; Gong, Y.; Dai, J.; Hamann, T. R.; Hu, L.et al. High-rate lithium cycling in a scalable trilayer Li-garnet-electrolyte architecture. *Mater. Today* **2019,** *22*, 50.
(15) Xu, S.; McOwen, D. W.; Wang, C.; Zhang, L.; Luo, W.; Chen, C.; Li, Y.; Gong, Y.; Dai, J.; Kuang, Y.et al. Three-Dimensional, Solid-State Mixed Electron–Ion Conductive Framework for Lithium Metal Anode. *Nano Lett.* **2018,** *18* (6), 3926.
(16) Yang, C.; Zhang, L.; Liu, B.; Xu, S.; Hamann, T.; McOwen, D.; Dai, J.; Luo, W.; Gong, Y.; Wachsman, E. D.et al. Continuous plating/stripping behavior of solid-state lithium metal anode in a 3D ion-conductive framework. *Proceedings of the National Academy of Sciences* **2018,** *115* (15), 3770.